ABSTRACT

Title of Thesis: ANALYSIS AND QUANTIFICATION OF HAZARDS ASSOCIATED WITH CASCADING THERMAL RUNAWAY PROPAGATION IN LITHIUM ION BATTERY CELL ARRAYS

Christopher P. Lee, Master of Science, 2018

Thesis Directed By: Associate Professor Dr. Stanislav I. Stoliarov, Department of Fire Protection Engineering

Lithium ion batteries are among the most common and efficient electrical energy storage devices despite the thermal, fire, and chemical hazards they pose upon thermal failure due to abnormal conditions. The hazards are intensified when thermal failure propagates from a single cell to neighboring cells in a battery pack. A new wind tunnel experimental setup was designed and built to investigate the dynamics, gaseous emissions, and energetics of cascading failure propagation in 18650 form factor, 2600 mA h, lithium cobalt oxide cathode cell arrays. Ambient environment (N_2 / air), cell state of charge (SOC; 50% / 100%), and cell arrangement (without 5 mm gaps between cell rows / with 5 mm gaps between cell rows) were all varied during tests to investigate different aspects of battery pack failure and quantify the impact of different failure mitigation strategies. On average, failure propagation speed was 7.5 times faster in air than in nitrogen, 8.5 times slower at 50% SOC than at 100% SOC, and three times

slower with a 5 mm gap between cells than without it. All tested cell arrays ejected minor mass yields of O_2 and H_2, as well as comparatively large mass yields of total unburned hydrocarbons, CO and CO_2. At 100% SOC, approximately 59 kJ of energy per cell was produced from the chemical reactions between cell components during failure. An additional 62.8 ± 18.4 kJ per cell was produced when the ejected battery materials during failure combusted in a reacting medium, but the combustion in the wind tunnel setup was highly incomplete due to the development of under-ventilated conditions. In a separate experimental setup with near complete combustion, combustion energy of 107 ± 17.7 kJ per cell was measured.

ANALYSIS AND QUANTIFICATION OF HAZARDS ASSOCIATED WITH CASCADING THERMAL RUNAWAY PROPAGATION IN LITHIUM ION BATTERY CELL ARRAYS

by

Christopher P. Lee

Thesis submitted to the Faculty of the Graduate School of the
University of Maryland, College Park, in partial fulfillment
of the requirements for the degree of
Master of Science
2018

Advisory Committee:
  Associate Professor Dr. Stanislav I. Stoliarov, Chair
  Professor Dr. Peter B. Sunderland
  Associate Professor Dr. Michael J. Gollner

Acknowledgements

I would be remiss not to first thank my advisor, Dr. Stanislav Stoliarov, and my research partner, Ahmed Said, for all of their assistance and guidance with this project. Dr. Stas, thank you for introducing me to this project and guiding me every step of the way. Learning from your technical expertise, hard work ethic, and attention to detail has helped me become an infinitely better researcher, but what I most want to thank you for is your ability to build my confidence and put me at ease. Every time I would go into your office for a meeting feeling stressed about slow progress and mounting work that needed to get done, I would somehow always leave with a clear sense of direction and feeling of optimism about the project. Ahmed, I cannot thank you enough for all of your guidance and support. Thank you for designing the setup, running every experiment with me, and answering any question I had. I do not think there is any way I could have completed this project on my own.

I would also like to thank United Technologies and the Transportation Research Board for sponsoring this project. In addition to the financial support, I would like to thank everyone who sat in on meetings and presentations and offered their thoughts on the project. Thank you all for taking the time to listen and give your input.

Special thanks also need to be given to Xuan Liu, whose research with Dr. Stas laid the foundation for the bulk of this project, as well as Jimmy Baldwin and Jordan Lanham, who both helped me with a lot of the preparation of experiments.

I would like to thank my committee members Dr. Peter Sunderland and Dr. Michael Gollner for taking the time to review my thesis. You both have been amazing mentors and resources for me in my five years here.

Additionally, I need to thank my other lab group members and friends in the department. It is because of you all that I look forward to coming into the office every day. As interesting as fire protection engineering is, I truly believe it is the people that make this department special.

Lastly, I thank my family for all of their love and support over the years. Through all the ups and downs, you all always encouraged and enabled me to live my best life. Thanks for instilling me with a love of learning and passion for everything I do. You all inspire me every day.

Table of Contents

List of Tables

List of Figures

List of Abbreviations

ARC: Accelerating rate calorimetry

CFD: Computational fluid dynamics

CSBC: Copper Slug Battery Calorimetry

DAQ: Data acquisition

DC: Direct current

DSC: Differential scanning calorimetry

FPA: Fire Propagation Apparatus

FTIR: Fourier-transform infrared spectroscopy

HRR: Heat release rate

LCO: Lithium cobalt oxide

LFL: Lower flammability limit

LIB: Lithium ion battery

PVDF: Polyvinylidene fluoride

SOC: State of charge

THC: Total hydrocarbons

Chapter 1: Introduction

1.1 Motivation and Background

Concerns associated with the negative environmental impact and sustainability of current energy sources have driven the need for clean, renewable energy sources [1-2]. Effective energy storage systems become increasingly necessary as the demand for renewable energy grows [1-2]. Lithium ion batteries (LIBs) are one of the most common energy storage devices due to their combination of light weight, long cycle life, high efficiency and energy density, lack of a memory effect, and portability [1-3]. Unfortunately, LIBs are relatively expensive, perform poorly at low temperatures, and most concerningly, pose significant safety hazards [2-5]. As LIBs are constantly being employed in an increasing number of applications, these safety concerns become paramount.

Single LIB cells consist of several components, but the four primary components are positive (cathode) and negative (anode) electrodes, electrolyte, and separator [2, 4]. In typical commercial LIB cells, the cathode material is a metal oxide ($LiCoO_2$, for example), and the anode material is carbon, most often graphite [2, 4]. The electrolyte is a lithium salt in an organic solvent typically made up of organic carbonates [2, 4]. The separator is a thin micro-porous polymer layer that separates the cathode and anode, allowing lithium ions to pass through between electrodes while also preventing internal short circuit [2, 4]. LIB cells are rechargeable, meaning that lithium ions can flow in both directions, from cathode to anode during charging and anode to cathode during discharging [2, 4].

For a multitude of reasons, including but not limited to short circuit, mechanical damage, overcharging, and external heating, LIB cells can fail irreversibly, resulting in extremely high temperatures, and potential fire and/or explosion [2-5]. This failure process can be characterized as having two distinct stages, referred to as safety venting and thermal runaway. Regardless the cause of failure, the initial increase in temperature causes vaporization of the electrolyte and decomposition of the separator, both of which produce flammable gases and build the internal pressure [3-4]. Once the internal pressure building within the cell reaches a certain point, vent ports on the cell casing open to relieve the pressure, eject gases, and prevent rupture [3-4]; this process is known as safety venting. Safety venting can be identified by an audible clicking associated with the ports opening and a visible, slow ejection rate of flammable gases [3-4]. As the temperature of the cell continues to increase, exothermic reactions between cell electrodes and electrolyte initiate [3-4]. The increasing temperature continually increases the chemical reaction rates inside the cell as well, resulting in rapid self-heating [3-5]. This cyclic heating feedback loop eventually causes the cell to reach its thermal runaway stage, wherein the temperature and ejection rate of the cell rapidly increase, often producing a fire [3-5]. Solid cell components can be ejected and cell casings can rupture during this stage as well [4].

A number of explosion and/or fire incidents have occurred in recent years as a result of LIB failure. These incidents range from cell phone explosions [6-7], to electric car fires [8], to the crashing and grounding of airplanes [9-10]. The hazards posed by LIBs have led to strict regulations on their transportation by airplane; spare, uninstalled LIBs are not currently allowed in checked passenger baggage and a maximum of two

LIBs greater than 100 W h are permitted in carry-on passenger baggage [11]. These incidents stress the importance of LIB safety and need for innovation both in their design and implementation.

1.2 Literature Review

1.2.1 Thermal Hazards Associated with Single Cell Failure

Several investigations have been conducted on the energetics of failure of individual LIB cells and cell components. These investigations have employed techniques such as differential scanning calorimetry (DSC) [12-16], accelerating rate calorimetry (ARC) [13, 16-19], and modified bomb calorimetry [20-21].

DSC has commonly been used to study the physical and chemical transitions of milligram-scale LIB components. Yang et al. [12] investigated graphite (a common anode material) with DSC at various states of charge (SOCs). Sharp exothermic peaks, attributed to the structural collapse of the graphite, were observed around 300 °C for samples containing more than 0.71 lithium ions per 6 carbons. It was also discovered that lithium ions released from the graphite reacted with a polyvinylidene fluoride (PVDF) binder (used to fix the active material containing lithium ions within the cathode), producing additional heat. Maleki et al. [13] used DSC to determine the thermal stability of Sn-$LiCoO_2$ cathode and graphite anode up to 400 °C. The total exothermic heat generation of the cathode and anode were determined to be 407 and 697 J g^{-1}, respectively. More recently, Duh et al. [14] used DSC to study the thermal stability of seven different cathode materials, all mixed with ethylene carbonate. The materials were all tested in both lithiated and delithiated states. Lithiated cathode materials were found to be more thermally stable that delithiated materials, exhibiting significantly greater onset temperatures.

ARC has been used to measure temperature and pressure changes inside a sealed metal test chamber caused by LIB thermal failure. Von Sacken et al. [17] used ARC to compare the thermal stability of different anode materials and found that a carbon intercalation anode was more thermally stable and predictable than a lithium metal anode, due to its ability to better maintain its structure. Maleki et al. [13] tested prismatic, Sn-$LiCoO_2$ cathode LIB cells with ARC to determine the onset temperatures of exothermic reactions. Reactions began to occur around 123 °C and thermal runaway initiated around 167 °C. The exothermic reaction and thermal runaway onset temperatures matched well with the thermal decomposition temperature ranges of the electrolyte and active cathode material, respectively. Similarly, Al Hallaj el al. [18] tested commercial LIBs at different open circuit voltages (corresponding to various SOCs) in an ARC to determine thermal runaway onset temperatures. Onset temperatures of 104, 109, and 144 °C were determined for cells with open circuit voltages of 4.06, 3.0, and 2.8 V, respectively, indicating that even a slightly charged cell (3.0 V) would fail much earlier than a fully discharged cell (2.8 V).

Lyon and Walters [20-21] recently conducted an investigation on four different cathode chemistry batteries using a modified inert atmosphere bomb calorimeter. Cell failure was initiated with electrical resistance heating and the total energy of failure of the cell was calculated. It was determined that the temperature rise during thermal runaway, total energy release, and volatile mass loss were all proportional to the stored electrical energy for various cathode types. Additionally, it was determined that the energy generated as a result of chemical reactions during failure was approximately two times the stored electrical energy for most cell chemistries.

While useful for characterizing failure energetics, DSC, ARC, and bomb calorimetry have significant limitations as it relates to LIB energetics research. None of these techniques were originally designed for LIB analysis or the extreme self-heating exhibited by LIBs. DSC is limited to milligram scale samples, meaning that cell components can only be tested individually and it is impossible to quantify how the cell acts as a whole. Additionally, none of these techniques quantify the dynamics of the failure process or distinguish between reactions occurring within and outside of the cell casing (after cell components have been ejected).

In order to circumvent these limitations, Liu et al. [22-24] recently developed a technique specifically designed for LIB testing, Copper Slug Battery Calorimetry (CSBC). CSBC allowed for careful measurement of the energy generated due to chemical reactions occurring inside the cell casing only. The technique involved inserting a cell into an insulated copper slug and heating it externally, in open atmosphere, to initiate its failure. A thermocouple was inserted into the copper slug and the temperature was taken as the homogeneous surface temperature of the battery, invoking a lump-capacitance assumption. 18650 form factor batteries with cathode chemistries of $LiCoO_2$, $LiNiMnCoO_2$, and $LiFePO_4$ were tested, all at SOCs of 0%, 25%, 50%, and 100%. For all cathode chemistries, the internal heat generation increased with increasing SOC up to 50%, but the values for 50% and 100% SOC were comparable for most cathode chemistries due to significantly greater ejected mass at 100% SOC. Quintiere et al. [25] conducted experiments with a similar custom thermal capacitance calorimeter, but expanded the investigation to include other form factors (cell geometries) and other types of batteries (including NiMH, NiCd, and lithium-metal primary cells).

1.2.2 Fire Hazards Associated with Single Cell Failure

In addition to the thermal hazards associated with energetics from cell chemical reactions, many studies have also been conducted on fire hazards associated with thermal runaway. Both Liu at al. [22-24] and Quintiere et al. [25] conducted experiments with a cone calorimeter to measure energy associated with flaming combustion of ejected combustible battery gases and components. Liu et al. conducted CSBC tests under the cone calorimeter and Quintiere el al. conducted cone calorimeter tests with a modified sample holder equipped with walls to prevent battery components from escaping. Both investigations experienced issues related to incomplete combustion for cells at 100% SOC, however. Many cathode chemistries experienced very fast ejection rates during thermal runaway of cells at 100% SOC. The high hydrodynamic strain rates associated with the turbulent flow caused intermittency of the flame, prevented many combustible gases from burning, and often damaged the ignitor, resulting in significantly underestimated flaming combustion energy values. To resolve this issue, Said et al. [26] modified the CSBC to include a stainless steel collector / burner tube, appended with a perforated plate, which slowed and homogenized the ejected gases during battery failure. This modification enabled significantly more complete combustion for 100% SOC cells. Prismatic, 1880 mA h, $LiCoO_2$ cathode cells were tested and the total flaming combustion energy for 100% SOC cells was found to be 113 kJ, compared to just 71 kJ for 50% SOC cells.

Other studies [27-30] have been conducted to quantify flaming combustion energy as well, typically using an oxygen consumption technique. Wang, Ping, et al. [27-28] conducted full scale fire tests on commercial 50 A h, $LiFePO_4$ cathode batteries to determine cell surface temperature, heat release rate, flame temperature, and mass loss rate. For these cells, thermal runaway onset temperatures as low as 127 °C, flame temperatures as high as 1500 °C, and total flaming combustion energy as high as 18.2 MJ were achieved. Additionally, the flaming combustion energy, mass loss, and peak heat release rate were all found to increase with increasing SOC. Ribière et al. [29] conducted combustion tests on pouch form factor cells at multiple SOCs in a Fire Propagation Apparatus (FPA) equipped with a Fourier-transform infrared spectroscopy (FTIR) instrument. Despite utilizing a different instrument, this investigation experienced similar incomplete combustion issues as Liu et al. [22-24] and Quintiere et al. [25], however.

1.2.3 Chemical Hazards Associated with Single Cell Failure

Other studies have focused on the chemical hazards associated with the hazardous gases that are produced and ejected during cell failure. In addition to studying the fire hazards, Ribière et al. [29] employed the FPA gas analyzers and FTIR to conduct additional analysis on gas concentrations in the exhaust stream. Many, but not all, of the gases ejected from the cells during failure combusted, so the measured concentrations consisted of both combustion products and gases ejected from the cells directly. CO, CO_2, SO_2 and total hydrocarbon (THC) production were all found to increase with increasing SOC, but HF production was found to decrease with increasing SOC. Similar studies [30-35] have been conducted on cells with many different specifications (form factor, cathode chemistry, capacity, etc.) to investigate the gas concentrations, and they concluded that significant concentrations of toxic products, particularly CO, HF, and POF_3, are produced.

Maloney [36] conducted gas analysis as well, but for cells tested in an inert environment, so any gas concentrations were known to have been produced from cell chemical reactions only, without any combustion. Cells of different cathode chemistries and SOCs were brought to failure through external heating inside of an inert atmosphere 21.7 L pressure vessel equipped with O_2, CO, CO_2, THC, and H_2 analyzers. It was determined that the overall ejected gas volume increased with increasing SOC. Lower flammability limit decreased with increasing SOC up to 40%, and then remained fairly constant afterward. The ejected gases from cells with $LiFePO_4$ cathodes were also significantly less flammable and smaller in volume than the gases ejected from other cells. Additionally, for $LiCoO_2$ cathode cells, volumetric concentrations of CO and H_2 were both found to increase from 5 – 10% to 20 – 30% for SOC greater than 50%. These volumetric concentrations represented all gases ejected from the cells, and when the fractions of CO and H_2 increased, the fractions of THC and CO_2 similarly decreased.

1.2.4 Experimental Work on Battery Pack Failure

Single LIB cells can pose serious hazards, but they are unable to provide the energy required to power most practical electric applications. Instead, battery packs made up of multiple cells electrically connected in either series or parallel are typically utilized. Unfortunately, battery packs present more significant safety concerns than single cells because of the potential for cascading failure, meaning the failure of one cell can initiate the failure of surrounding cells that rapidly propagates throughout the cell arrangement [4]. This propagating failure is primarily driven by the transport of thermal energy [4].

While thermal behavior of battery packs under different conditions (cell arrangement, cooling strategy, etc.) has been studied fairly extensively [37-40], none of these investigations studied cells undergoing thermal runaway. However, limited research has been conducted on LIB pack failure as well [28, 41-43]. Lopez et al. [41] investigated battery packs with different cell spacings, tab configurations, and vent locations. Results indicated that increasing cell spacing significantly decreased cell temperatures and minimized the chance of thermal runaway propagation, and a spacing of at least 2 mm was recommended. Branched style tabbing and upward facing vent locations were also found to reduce the overall damage caused by thermal runaway, when compared to serpentine style tabbing and side facing vent locations. Additionally, authors provided introductory work related to installing radiant barriers and intumescent materials in between cells, and found promising results in regards to preventing failure propagation. Lamb et al. [42] investigated the impact that cell form factor and electrical connectivity have on the failure propagation process. Pouch cells were found to propagate failure much quicker than cylindrical cells due to the greater conduction heat transfer from larger contact surface areas between cells. Additionally, parallel electrical configurations were found to propagate failure much faster and more often than series electrical configurations. Feng et al. [43] studied temperature, voltage, and heat transfer responses to nail penetration induced thermal runaway in prismatic, six cell packs. Results showed lower thermal runaway onset temperatures and shorter failure triggering times than ARC tests on identical single cells due to the introduction of side heating from adjacent cells. A maximum temperature increase of 792 °C was observed for cells within the pack. Additionally, heat transfer from pole connectors and the developed fire were found to be minimal in comparison to the heat transfer through the battery shell, indicating that conduction was the primary mode of heat transfer.

None of the previous studies on failing LIB packs provided thorough results on the dynamics of the cascading failure process. Liu [24] conducted introductory experiments on this topic by testing a six cell triangular array in both air and nitrogen environments. Through video and thermocouple measurements, thermal runaway onset times were recorded for each cell in the array, and the recorded times were used to determine the propagation speed. Liu found that the failure propagated much faster from the second row to the third row than it did from the first row to the second row, indicating an accelerating failure propagation.

1.2.5 Modeling Work on Battery Pack Failure

In addition to experimental studies, modeling work has been conducted on LIB pack failure as well [24, 44-48]. Feng at al. [44-45] expanded upon their previous work [43] and built a 3D thermal runaway propagation model based on energy balance equations. Empirical equations based on their DSC and ARC data were used to simplify the chemical kinetics calculations, and equivalent thermal resistant layers were used to simplify the heat transfer between thin layers with complex geometries. The model determined that thermal runaway propagation could be postponed or prevented by modifying the separator to increase failure onset temperatures, discharging the cells to reduce the total energy release, increasing the convection coefficient to enhance the heat dissipation, or using thermal insulation layers to reduce cell-to-cell heat transfer. Experiments were conducted to validate all of these findings as well. Wang et al. [46] utilized 3D computational fluid dynamics (CFD) modeling to study the impact of cell arrangement and forced air-cooling strategies on battery pack failure. Results showed that forced air-cooling significantly reduced the temperatures of battery modules and that cooling was most effective when directed at the top of the battery pack. Additionally, a 5 by 5 square arrangement of LIB cells was found to best optimize cost and cooling capability, in comparison to 1 by 24 rectangular, 3 by 8 rectangular, 19 cell hexagonal, and 28 cell circular arrangements. The 19 cell hexagonal arrangement was found to best optimize space utilization, however. Liu [24] built a 3D thermal runaway propagation model in COMSOL Multiphysics to predict thermal runaway onset times for each cell in an array tested in nitrogen (combustion was not taken into account). The model was validated against his experimental temperature measurements and was able to predict his experimental onset times within 13%.

1.3 Project Scope and Objectives

Previous studies have not expanded careful quantification of gaseous emissions and failure energetics from single cells to cell arrays, nor have they monitored the dynamics of cascading failure across each individual cell. The purpose of this study was to accurately quantify and understand the various hazards that LIB packs pose and the fundamental processes that govern them. Combining simultaneous measurement of the dynamics, gaseous emissions, and energetics of LIB pack failure into a single experimental setup was a key objective of this research. The setup was also designed to maintain variable, well-defined conditions to allow for proper and thorough interpretation of all failure phenomena. Most tests were conducted in nitrogen to accurately quantify species yields and energy generated directly from chemical reactions between cell components. Other tests were conducted in air to investigate the propagation impact and energetics of combustion, and to simulate a more realistic scenario for a battery pack. Lastly, SOC and cell arrangement were modified to study how these parameters affect the hazards posed by LIB packs and how effective they are as mitigation strategies. These tests were conducted to provide optimized introductory recommendations for safer battery pack design, transportation, and storage.

Chapter 2: Experimental Setup and Procedures

2.1 Test Samples

Tenergy ICR18650 LIB cells were examined for all tests in this study. These cells have an 18650 form factor, meaning they are cylindrical in shape, 18 mm in diameter, and 65 mm in height. Figure 2.1 provides an image of a cell with and without its plastic packaging, and Table 2.1 provides detailed specifications of the cell. The form factor and cathode chemistry of the cells are commonly used in applications, and the nominal capacity of the cells is near the upper limit of what is commercially available for 18650, lithium cobalt oxide (LCO) cathode cells

Figure 2.1: Tested LIB cells with (left) and without (right) packaging.

Table 2.1: Specifications of Tenergy ICR18650 LIB cells [49].

Cathode material	Lithium cobalt oxide
Anode material	Carbon
Form factor	18650
Nominal capacity [mA h]	2600
Nominal voltage [V]	3.7
Maximum charge voltage [V]	4.2
Number of safety vent ports	4
Mass without plastic packaging [g]	43.57 ± 0.03

An iCharger 208B battery charger was used to charge cells to a specific SOC. Each cell was first cycled three times according to manufacturer recommendation. After this, each cell was fully discharged to a minimum voltage of 2.75 V with a constant current of 1.3 A. Then, each cell was fully charged to 4.20 V using the constant current (1.3 A) / constant voltage method until the current fell below 0.1 A. Lastly, for tests with 50% SOC cells, each cell was discharged with a constant current of 1.3 A until 50% SOC was reached, as calculated by current integration. The stored electrical energy of a cell was calculated during a discharge by integrating the product of the cell voltage and the discharge current, which were both tracked over time by the charger. At 50% and 100% SOC, average cell stored electrical energy was determined to be 15.5 ± 0.2 and 34.1 ± 0.3 kJ, respectively. The uncertainties associated with these averages, as well as the uncertainty associated with the mass average in Table 2.1, were calculated from the scatter of the data as two standard deviations of the mean.

2.2 Experimental Setup – Cell Array Tests

The experimental setup described herein was designed and built with the goal of investigating cascading thermal failure in LIB cell arrangements within a well-defined ambient environment. A schematic of the main experimental facility is shown in Figure 2.2. The setup consisted of six main sections: gas handling system, mixing chamber, pre-test section, test section, diagnostics section, and sampling system. Many sections consisted of large stainless steel ducts that were connected to each other with bolts and sealed along their flanges with RTV silicon gaskets to assemble a wind tunnel setup. All six of these sections are described in detail in the following subsections. The test section was the fourth section in sequence, but it is discussed first as the design of other sections primarily depended on its design.

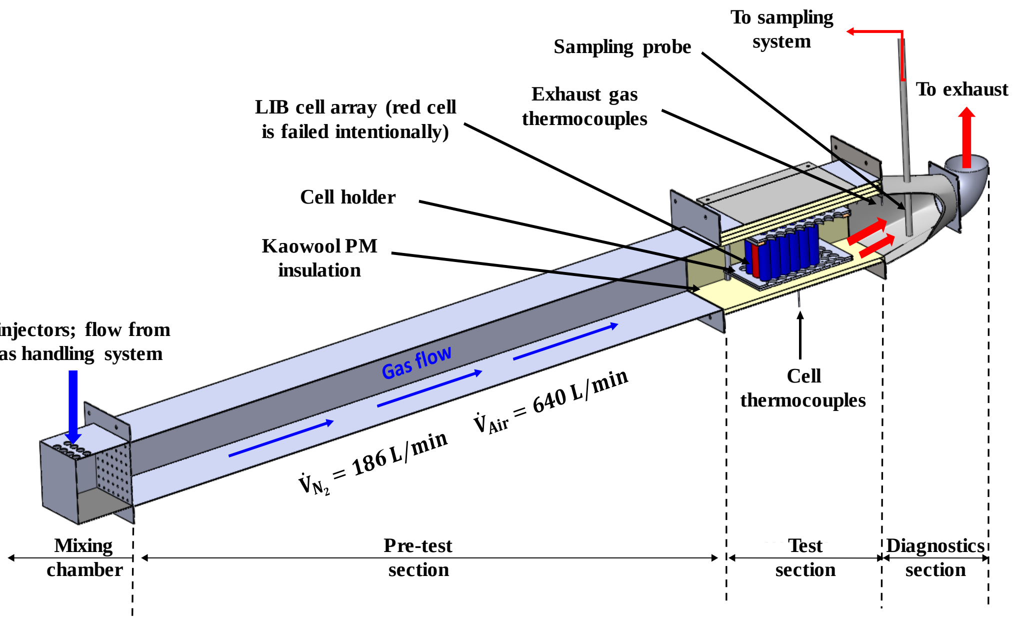

Figure 2.2: Schematic of the main experimental facility.

2.2.1 Test Section

All of the tested battery cell specimens were placed in this section. It was necessary to secure the cells in place during their failure processes to maintain the desired arrangement. A custom stainless steel holder was designed for this purpose. The holder consisted of two plates that secured up to 40 cells (in a 5 by 8 arrangement) in place on their top and bottom surfaces. Both plates were 120 mm wide by 174 mm long. The top plate was approximately 6.5 mm thick and the bottom plate was approximately 8 mm thick. The bottom plate had 40 circular depressions cut into it, each of 18 mm diameter and 4.5 mm depth. 3.2 mm thick Kaowool PM insulation discs were placed into each of the depressions, and cells were positioned in each of the depressions on top of the insulation. In addition, 3.5 mm diameter holes were drilled through the bottom plate and insulations disks at the center of each depression. A 24 gauge, silica yarn insulated, K-type thermocouple was fed through each of the holes and the beads were positioned in between the insulation discs and the bases of the cells to measure cell temperatures. Nationals Instruments DAQ hardware and Labview software were used to record these temperatures at a frequency of 2 Hz. 40 holes of 12 mm diameter were drilled through the top plate, each centered directly above the depressions in the bottom plate. These holes allowed the safety vent ports on the cells to eject gases freely, preventing pressure buildup and possible rupture. The top plate was also fully insulated on its bottom surface with 3.2 mm Kaowool PM. Insulating the top and bottom plates both limited conduction heat transfer from the cells to the plates and prevented any possible short circuiting. The two plates were secured with four long bolts in their corners. Lastly, the bottom surface of the bottom plate was equipped with four, 1 cm long, hollow, threaded, hexagonal struts in each corner. A labeled photograph of the cell holder is shown in Figure 2.3.

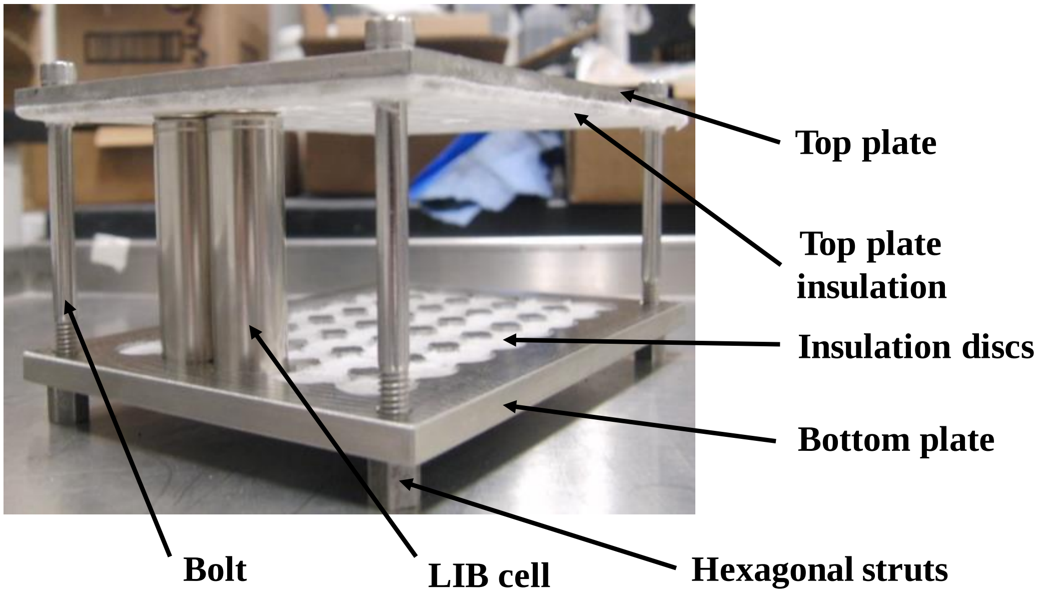

Figure 2.3: Labeled photograph of the cell holder outlining key features.

The cell holder shown in Figure 2.3 was designed to position cells back-to-back, with no inter-cell spacing, in a square packing arrangement. This arrangement was desired for most tests, but one set of tests (detailed in subsection 2.4.1) was conducted with different cell spacing conditions, so the top and bottom plates were slightly modified. A schematic of the modified bottom plate is shown in Figure 2.4. For these tests, 5 mm wide gaps were imposed before the fourth row and the fourth column of cells.

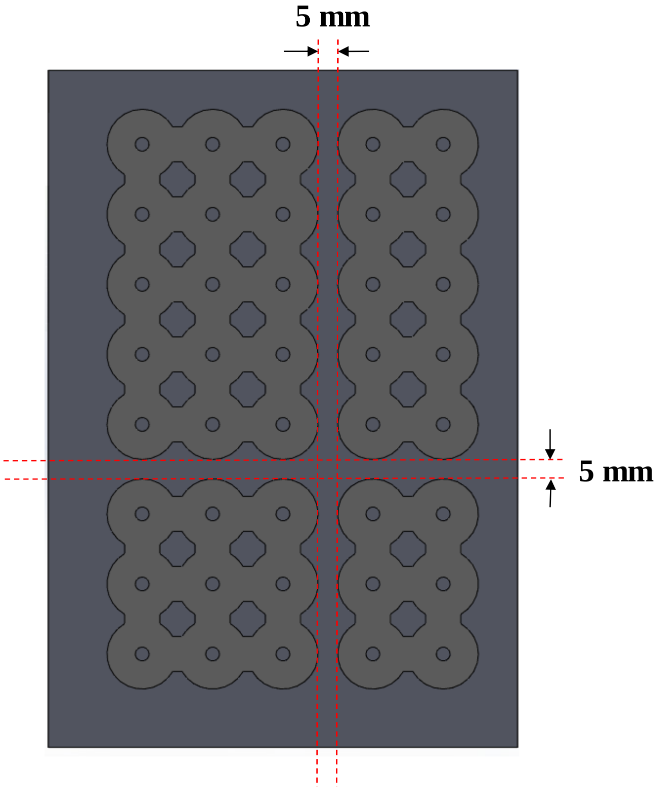

Figure 2.4: Schematic of the modified cell holder bottom plate for tests with 5 mm gaps.

For the tests with no gaps, thermal failure of the middle cell in the first row was initiated with external heating, and for the tests with gaps, thermal failure of the cell in the second column and first row was initiated with external heating (see Figure 2.14). External heating was provided by custom surface heaters made of a nickel-chromium resistive heating wire coiled back and forth between two pieces of high-temperature fiberglass cloth tape. The wire was supplied up to approximately 110 W by an external BK Precision DC power supply. The heaters were designed to be 65 mm tall (the same height as the cells) and cover approximately 45% of the cells' sidewall surface area. While the front side of the heater was in contact with the trigger cell, the back side was insulated with a Kaowool PM insulation piece. The heater and insulation piece were secured between the battery and a stainless steel support that was welded to the bottom plate of the cell holder. A schematic showing the full cell holder assembly, with the heater setup, is shown in Figure 2.5.

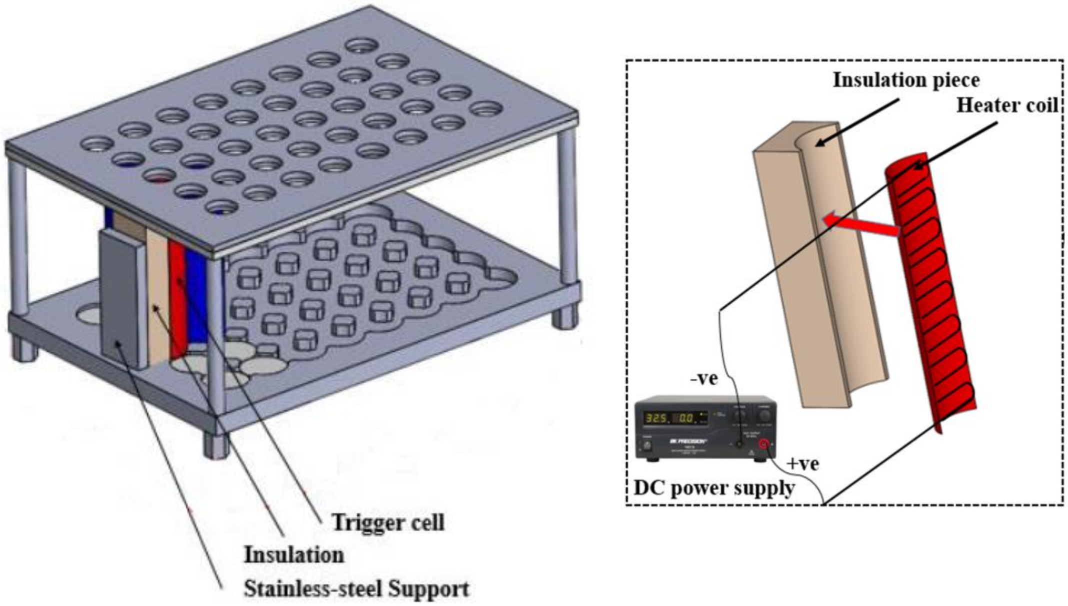

Figure 2.5: Labeled schematic of the surface heater setup within the cell holder.

The cell holder was fixed within a stainless steel duct with four screws coming in from the bottom surface of the duct into the hexagonal struts of the bottom plate. The top surface of the duct was removable to allow access to the cell holder in between tests. During tests this cover was bolted together with the rest of the duct. All internal surfaces of the duct were thermally insulated with Kaowool PM, having a 6.4 mm layer on the sides and bottom, and three 6.4 mm layers on the top. The top surface was directly exposed to the hot gases ejecting from the cells, so the additional layers were added. Lastly, a wire mesh (8 mm by 8 mm mesh size) was installed at both the inlet and outlet of the test section to prevent any large particulates or battery materials from traveling into the other sections of the experimental facility. Labeled schematics and photographs of the test section are shown in Figure 2.6.

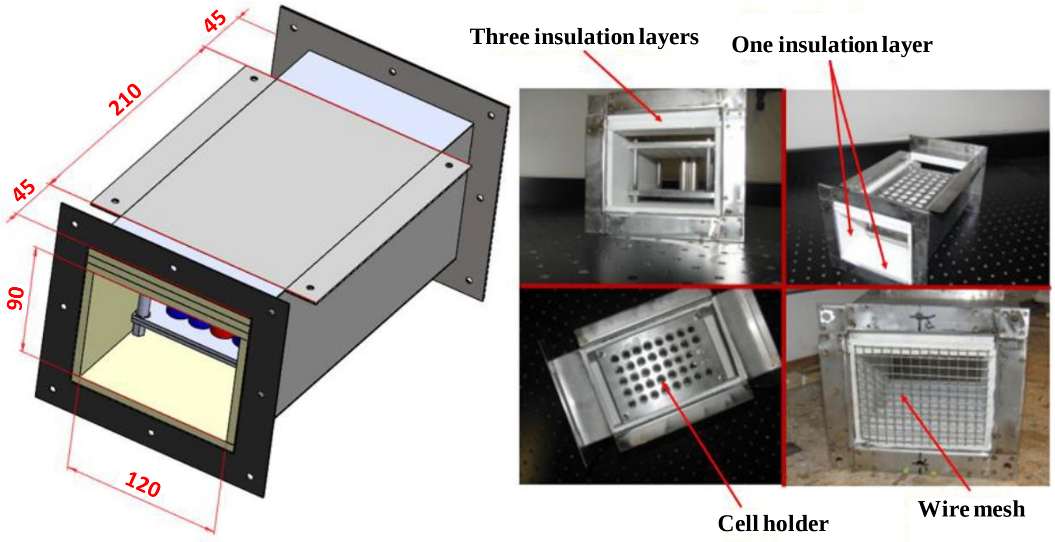

Figure 2.6: Dimensioned (in mm) schematic of the test section (left), and labeled photographs of the test section outlining key features (right).

An internal open cross section of 90 mm tall by 120 mm wide was designed for the test section. The 90 mm height allowed for 10 mm separations between the cell holder and the upper and lower insulation layers of the test section. The 120 mm width was equal to the width of the cell holder.

2.2.2 Gas Handling System

The gas handling system supplied and controlled the ambient environment surrounding the cell arrangement. Tests were conducted either in a pure nitrogen or air environment. Nitrogen provided inert ambient conditions where no combustion occurred and all heat and gases generated directly from the chemical reactions between battery components. Air provided reacting conditions where combustion was possible, representing a more realistic failure scenario.

For the nitrogen tests, the gas was supplied from a high-pressure nitrogen tank and passed through a pressure regulator to reduce the pressure of the stream before flowing through an Alicat mass flow controller. For the air tests, the flow was supplied from a compressor and passed through a desiccant filter / dryer to capture any particles or moisture in the stream before flowing through the mass flow controller. The mass flow controller was set at 186 L min^{-1} for the nitrogen tests and 640 L min^{-1} for the air tests. The nitrogen flowrate was chosen because it was the lowest flowrate that provided an oxygen concentration near zero in the duct. The air flowrate was chosen because it was the maximum flowrate that did not exceed a flow velocity in the pre-test section of 1 m s^{-1}. Furthermore, this flow velocity is typical for cooling conditions reported in previous publications [37-39, 46] and allowed the conditions inside the wind tunnel to be as well-ventilated as possible. After passing through the mass flow controller, the gas flow was directed to an aluminum rectangular manifold with eight outlets. The outlets were all equipped with flexible tubing that led to the mixing chamber. The purpose of this manifold (along with the entirety of the mixing chamber section) was to allow for thorough mixing of the flow stream before it reached the cells. A schematic of the entire gas handling system is shown in Figure 2.7.

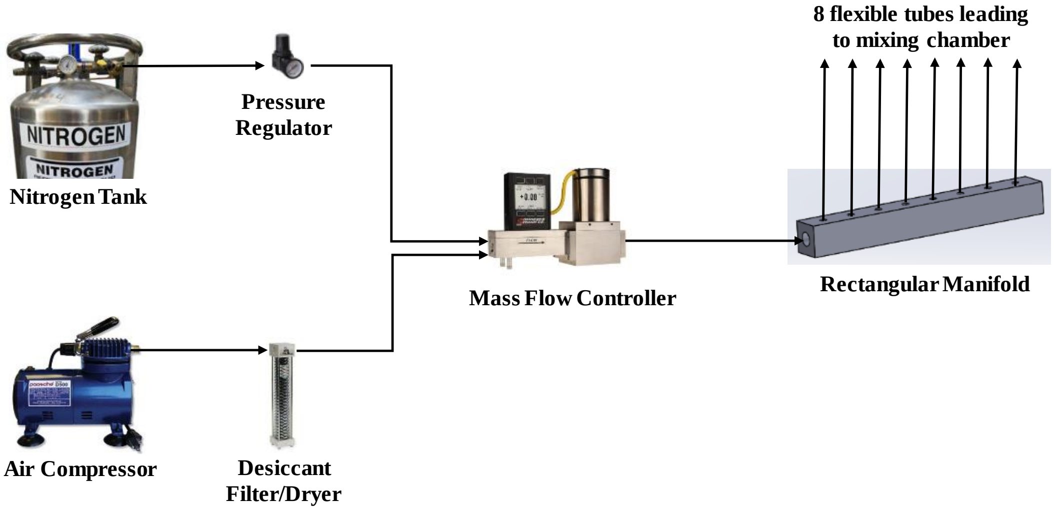

Figure 2.7: Schematic of the gas handling system.

2.2.3 Mixing Chamber

The mixing chamber was designed to thoroughly hydro-dynamically mix the injected gas before it reached the cells. The mixing chamber itself consisted of a small rectangular duct that was only open on one end. Eight injector holes were drilled into the duct's top surface and the flexible tubes coming from the manifold were attached. The open end of the duct was fitted with a custom aluminum perforated plate to achieve a significant pressure drop and better mixing. This plate had an open area of 4.6% which resulted in an upstream pressure 4.2 times greater than the downstream pressure. This pressure drop was significantly greater than the dynamic pressure inside the mixing chamber, which created a spatially uniform velocity downstream of the plate. A schematic and photograph of the mixing chamber are shown in Figure 2.8.

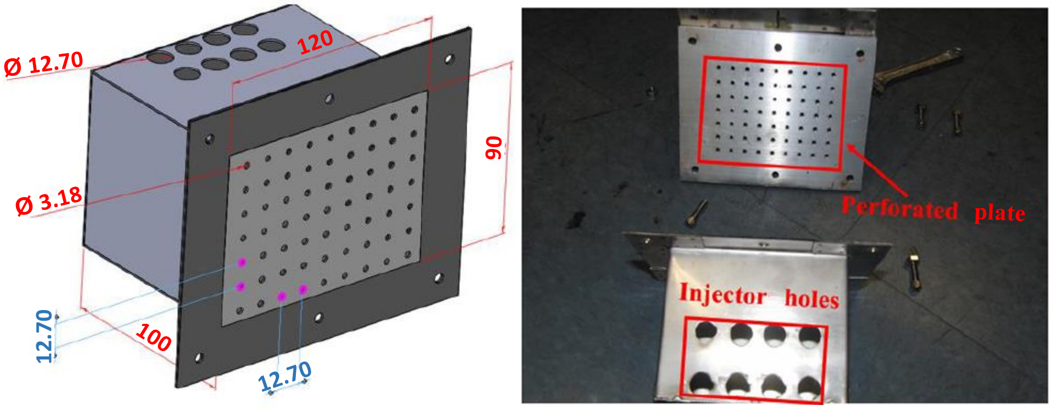

Figure 2.8: Dimensioned (in mm) schematic of the mixing chamber (left), and labeled photograph of the mixing chamber outlining key features (right).

2.2.4 Pre-Test Section

The pre-test section consisted of a long stainless steel duct and its purpose was to allow the air flow to fully develop before reaching the test section. The required hydrodynamic entry length, L_h, was determined based upon whether the flow was laminar or turbulent. With the known cross section (90 mm by 120 mm) and maximum air velocity (1 m s^{-1}), the Reynolds number, Re, was calculated to assess the nature of the flow. This calculation is described in Equations 2.1 and 2.2.

$$Re_D=\frac{uD_h}{v} \tag{2.1}$$

$$D_h=\frac{4A_c}{P} \tag{2.2}$$

Here, u is the maximum flow velocity, D_h is the hydraulic diameter of the duct, v is the kinematic viscosity of the flow (1.59E-5 m^2 s^{-1} for air at typical ambient temperature), A_c is the cross section of the duct, and P is the wetted perimeter of the duct. The hydraulic diameter was computed to be 103 mm.

Fully-developed turbulent flow was not developed for the nitrogen tests, but Reynolds number of approximately 6500 was calculated for air, which indicated turbulent flow [50]. For turbulent flow, the minimum hydrodynamic entry length can be approximated as $10D_h$ [50]. Therefore, the pre-test section length was designed to be 1100 mm. A schematic of the pre-test section is shown in Figure 2.9.

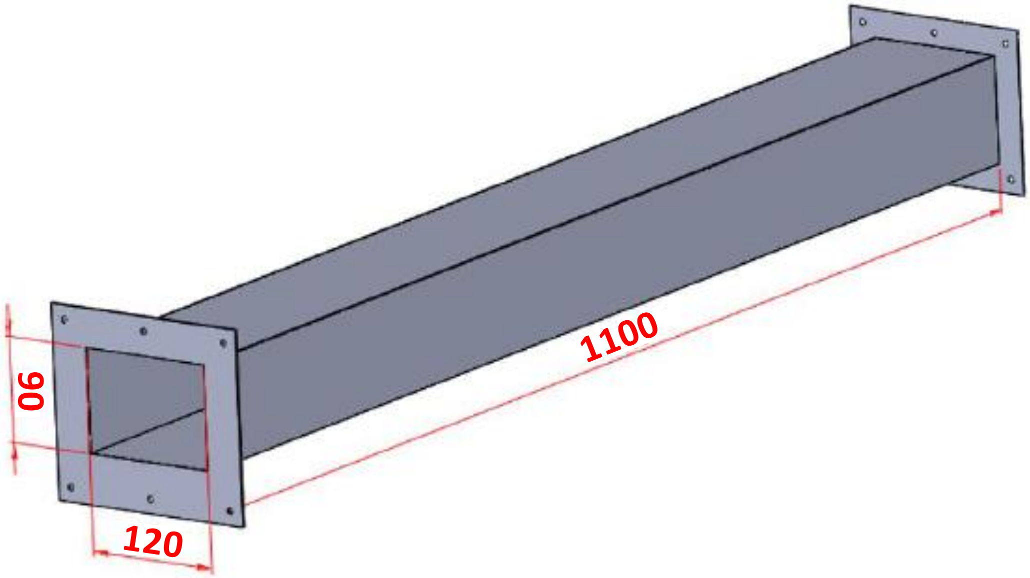

Figure 2.9: Dimensioned (in mm) schematic of the pre-test section.

2.2.5 Diagnostics Section

The diagnostics section consisted of a conical stainless steel duct that was connected downstream of the test section. The internal surfaces of the duct were lined with 6.4 mm Kaowool PM insulation layers. Additionally, a stainless steel exhaust elbow was connected to the end of the diagnostics section to direct the exhaust flow up towards an exhaust hood.

15 mm back from the inlet of the diagnostics section, three sheathed, 1 mm diameter, K-type thermocouples were inserted into the duct through the top surface to

measure the exhaust gas temperature. Due to the violent and turbulent nature of LIB failure, it was not assumed that the exhaust stream would be hottest near the top of the duct, so the three thermocouples were all placed at different heights within the open cross section to obtain an average temperature. The three thermocouples were positioned 46, 36, and 17.5 mm down from the bottom surface of the top insulation layer, respectively. The thermocouples sampled the exhaust gas temperature at 2 Hz.

Additionally, a custom-made sampling probe was designed to sample the gas flow downstream of the cells. The probe consisted of a 9.5 mm diameter stainless steel tube that was completely closed on one end and connected to the sampling system on the other end. The gas was sampled through two longitudinal columns of 1 mm diameter perforations in the probe. These perforations were located on the side of the probe opposite of the incoming flow to avoid clogging from solid particulates. A schematic and photograph of the entire diagnostics section is shown in Figure 2.10, and a schematic of a cross section within the diagnostics section is shown in Figure 2.11.

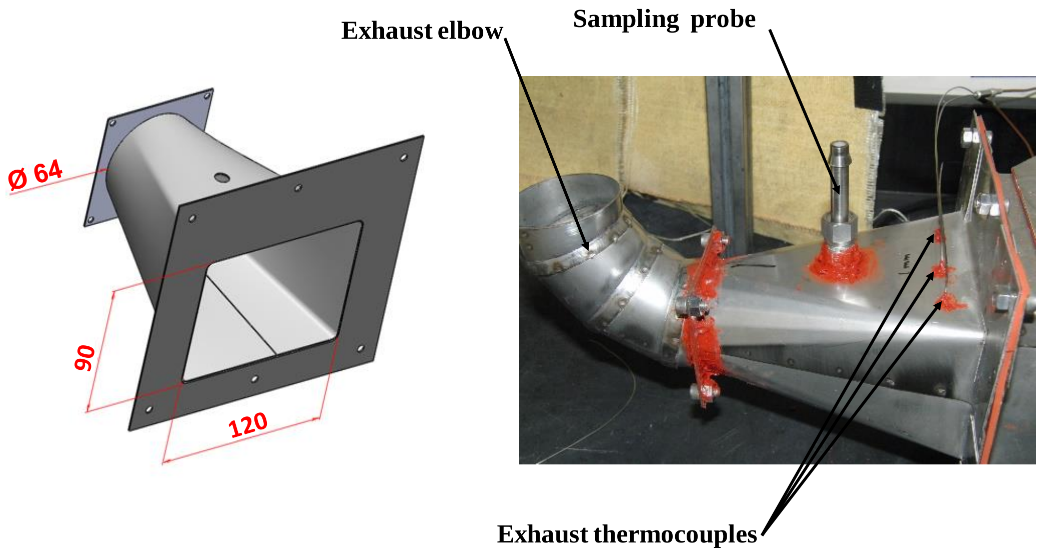

Figure 2.10: Dimensioned (in mm) schematic of the diagnostics section (left), and labeled photograph of the diagnostic section outlining key features (right).

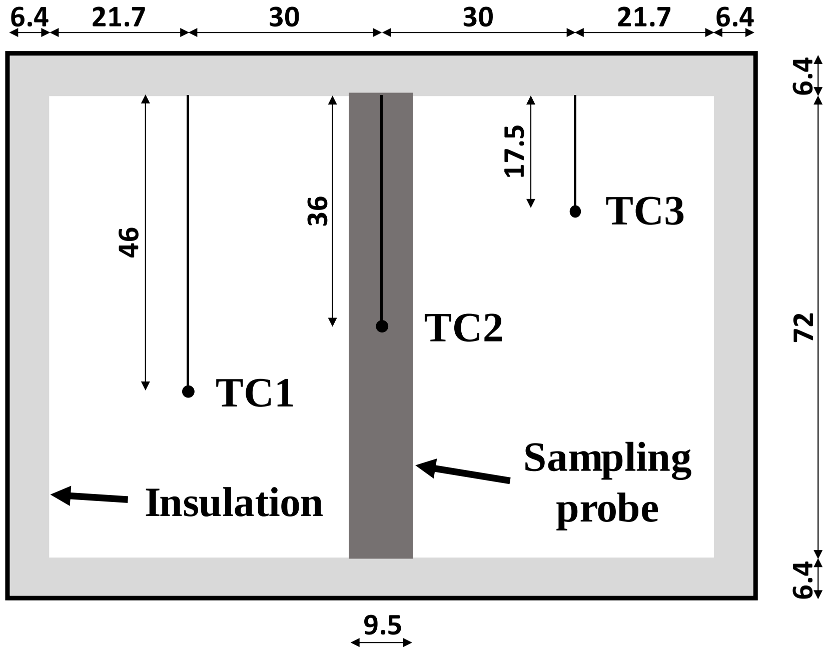

Figure 2.11: Dimensioned (in mm) schematic of the vertical cross section within the wind tunnel along the plane of the exhaust gas thermocouples. While visible in this view, the sampling probe is positioned 60 mm behind the thermocouples.

2.2.6 Sampling System

From the sampling probe, gas samples were drawn at a rate of 5 L min^{-1} using a Boxer diaphragm double head pump. Before reaching the pump itself, the sample gas passed through a disposal coalescing soot filter and a Drierite filter. The soot filter removed solid particulates as small as 0.01 microns at 95% efficiency and the Drierite removed any moisture from the stream. Additionally, the tubing material, diameter, and distance between the sampling probe and pump was selected to ensure that the temperature of the gases entering the pump (and subsequently the gas sensors) did not exceed 320 K. The pump had two outlets and both of the outlet streams were split in two to produce four gas streams, each directed toward a rotameter. The rotameters were utilized to regulate the flow entering each sensor down to 1.25 L min^{-1}. This sampling flow rate was within the recommended range for each sensor.

The gas sensors employed included an electrochemical fuel-cell type automotive oxygen sensor (“Teledyne R17-a”), total unburned hydrocarbons, carbon monoxide, and carbon dioxide infrared sensors (“Edinburgh GasCard NG”), and a thin film palladium-nickel alloy hydrogen sensor (“HY-OPTIMA 700B Series”). All sensors were installed in parallel (each being fed by its own rotameter), with the exception of the hydrogen sensor, which was installed in series after the carbon monoxide sensor. The hydrogen sensor was unused during the air environment tests because manufacturers recommended not exposing it to O_2 concentrations greater than 5 vol. %. All of the sensors were sampled at a frequency of 2 Hz with National Instruments DAQ modules and Labview software. After passing through the sensors, all gas streams were directed towards an exhaust hood. A schematic of the entire sampling system is shown in Figure 2.12.

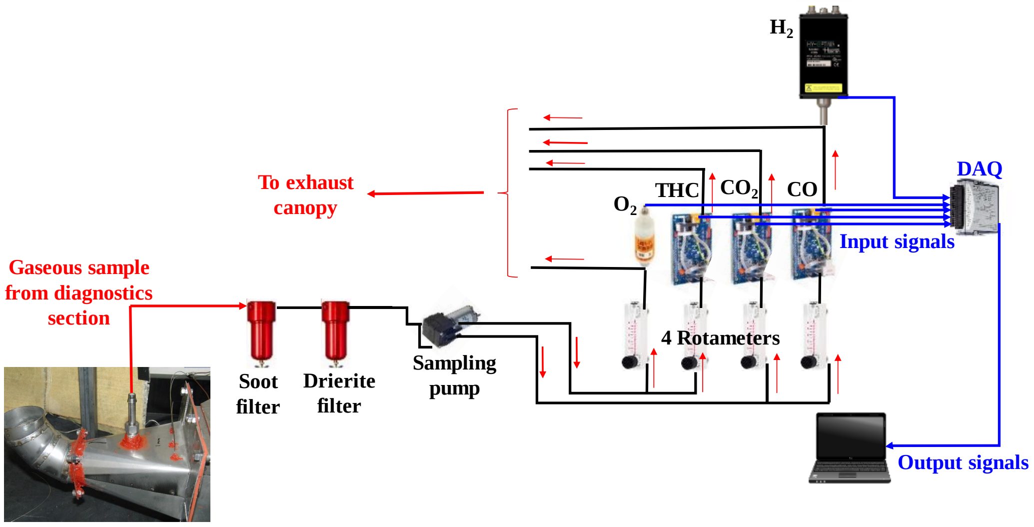

Figure 2.12: Schematic of the sampling system.

2.3 Experimental Setup – CSBC / Cone Calorimeter Tests

A second experimental setup was utilized to obtain additional flaming combustion energy data. In these tests, Copper Slug Battery Calorimetry (CSBC) [22-24, 26] was combined with a standard Govmark cone calorimeter [51] to measure heat release rate (HRR) based on oxygen consumption. Full CSBC details are provided by Liu [22-24], but in general, the setup consisted of a cylindrical copper slug with an 18 mm diameter hole that an 18650 form factor LIB cell fit perfectly inside of to ensure direct thermal contact between the copper and cell sidewalls. The copper slug was wrapped in a nickel-chromium heating wire being supplied with 40 W by an external DC power supply, and surrounded by a 200 mm diameter layer of thermal insulation. The whole CSBC apparatus was placed under an ignitor in a cone calorimeter to track HRR over time as the cell failed.

Liu et al. conducted similar experiments [22-24], but one key difference in this work was the addition of an ejected battery material collector / burner, developed and outlined by Said et al. [26]. The collector / burner consisted of a 75 mm diameter and 150 mm tall stainless steel tube attached to the top surface of the CSBC. A perforated stainless steel plate was attached to the other end of the tube and a hot wire ignitor was positioned just above the plate to ignite all escaping flammable gases. Liu et al. did not use the collector / burner and instead positioned the ignitor just above the top surface of the cell [22-24]. Without the collector / burner, the ejection rate from LCO cells during thermal runaway was sufficiently fast that the ignitor often broke and not all flammable gases were ignited. Furthermore, the ignitor subjected the cell to additional undefined heat with this setup. The collector / burner effectively slowed and homogenized the flow before reaching the ignitor, resulting in a significantly more complete combustion. The collector / burner also provided sufficient distance between the ignitor and the cell such that the heating influence from the ignitor was negligible. The CSBC tests were repeated five times to accumulate statistics. A schematic of the CSBC setup is shown in Figure 2.13.

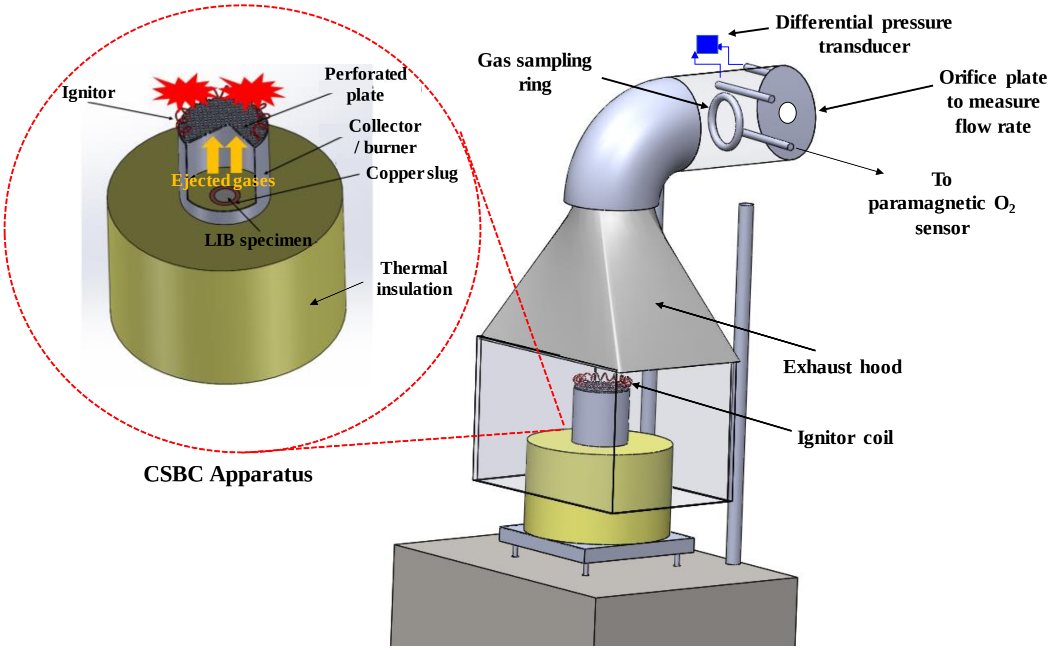

Figure 2.13: Labeled schematic of the CSBC test setup.

2.4 Test Procedures

2.4.1 Cell Array Tests

Four different sets of tests were conducted, as described by Table 2.2.

Table 2.2: Test matrix of completed experiments.

Number of completed tests	**Ambient environment**	**Number of cells**	**SOC of all cells [%]**	**Gap width before fourth row and fourth column [mm]**
4	N_2	12	100	0
4	Air	12	100	0
4	N_2	12	50	0
4	N_2	15	100	5

The 12 cell, 100% SOC tests in nitrogen and air were conducted as baseline experiments. The nitrogen tests were conducted to determine the ejected gas yields and energy production from the cells themselves. The air tests were conducted to investigate a more realistic failure scenario where flame and combustion processes influence the failure behavior. The N_2 and air volumetric flow rates result in bulk velocities across the 12 cell arrays of approximately 0.6 and 2.2 m s^{-1}, respectively.

After the baseline tests, the 12 cell, 50% SOC and 15 cell, 100% SOC, 5 mm gap test sets were conducted to investigate different LIB pack failure mitigation strategies. Both of these tests sets were conducted in a nitrogen environment to provide the best chance at preventing failure propagation throughout the cell array. The 50% SOC tests were conducted because battery packs are typically transported at decreased SOCs as an added level of protection [52]. The 5 mm gap tests were conducted to begin investigating how different cell arrangements within a battery pack affect the failure propagation from cell-to-cell. 5 mm was chosen as the gap width because it is roughly the largest cell separation thickness utilized in applications [48]. Gaps were only introduced before the fourth row and fourth column, instead of between every individual cell, for three reasons. First, a significant thermal mass was desired to test the impact of the gap under a worst-case failure scenario. As shown in Figure 2.14, the initial three by three block of cells, all in direct contact with each other, provided this thermal mass. Second, the limited number of gaps provided a more realistic cell arrangement of an actual battery pack. Cells within battery packs are typically arranged in groups or modules [2, 4]. Third, providing gaps between every cell would have dramatically increased the overall volume of the cell array, which is undesirable in typical applications.

Before each test, the inside of the wind tunnel setup and sampling system lines were all thoroughly cleaned, soot and Drierite filters were replaced, gas sensors were all calibrated with a zero point and at least one span point, cells were charged to the specified SOC, and cells were all weighed individually without their plastic packaging. After this, the cells were placed into the cell holder in an arrangement shown in Figure 2.14.

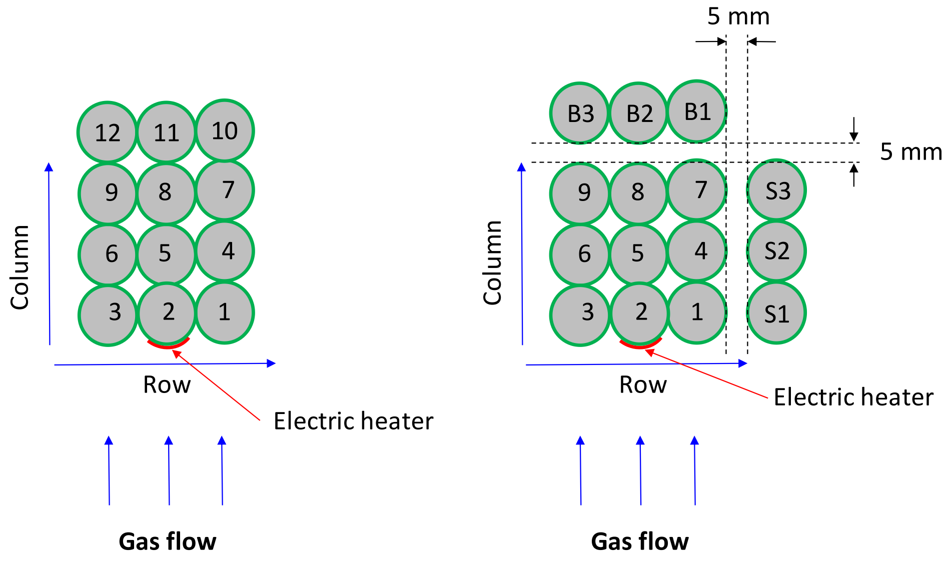

Figure 2.14: Cell arrangements for all tests conducted. All tests with 12 cells were arranged as shown on the left; all tests with 15 cells were arranged as shown on the right.

The heating element was positioned in contact with cell #2 for all tests. After placing the cells and heater, the top cover of the test section was attached and sealed, the ambient gas was introduced to the wind tunnel and allowed to flow for seven minutes prior to the test to homogenize the conditions in the test section, the rotameters for the gas sensors were set to 1.25 L min^{-1}, and the test was begun by starting the data acquisition and setting the power supply to approximately 110 W. This power supplied a heat flux to cell #2 of approximately 66.5 kW m^{-2}. During tests, safety venting and thermal runaway onset times were recorded by stopwatch based on the operators' observations (these observations are elaborated on in section 3.1). Additionally, the input power was monitored during each test and any changes were recorded. Tests were concluded and all systems were shut down after all battery failure processes concluded and the cell temperatures returned to their initial values. After each test, the cells were removed from the wind tunnel and individually weighed once again, and the positions of any ruptured cells were identified and recorded.

2.4.2 CSBC / Cone Calorimeter Tests

Single cells were investigated for the CSBC tests. These cells were charged to 100% SOC, weighed, and then placed into the copper slug such that the top surface of the cell was flush with the top surface of the slug and surrounding insulation. With the cell positioned, the collector / burner was attached and the CSBC apparatus was placed under the cone calorimeter with the ignitor positioned directly above it. Tests were begun by starting the cone calorimeter data acquisition, power supply, and ignitor all at once. The power supply was set to 40 W for all tests. The input power was less in the CSBC tests than in the wind tunnel tests because only the combustion energetics were measured and the slower heating promoted a more gradual ejection rate, leading to a more complete combustion. It is important to note that the cone calorimeter heater was not used for these tests (nor was the cone calorimeter mass balance), and instead all heating was supplied by the heating wire wrapped around the copper slug. Safety venting and thermal runaway onset times were manually recorded using a stopwatch. Tests were concluded after the cell had fully failed and the HRR trend had returned to its baseline value. After each test, the cell was weighed once again to determine its total mass loss.

Chapter 3: Data Analysis Methodology

3.1 Identification of Onsets and Ends of Safety Venting and Thermal Runaway

At the onset time of safety venting, t_{SV}, the cell temperature began to decrease slightly, before continuing to increase. This endothermic reaction peak is speculated to be associated with the vaporization of the electrolyte [3, 22-24, 26]. Therefore, the onset time of safety venting was defined as 0.5 s before the cell temperature derivative, $dT_{cell}\ dt^{-1}$, first fell below zero (0.5 s is the resolution of the thermocouple measurements). It is also important to note, however, that the safety venting onset was not clearly identified for many cells, especially 100% SOC cells in rows 2, 3, and 4. Typically, after the first few cells underwent thermal runaway, the rest of the cells in the array began to quickly undergo thermal runaway one after another. At this point, the individual safety venting onsets became indistinguishable in the cell temperature trends because they occurred at the same times as the thermal runaway onsets.

The onset time of thermal runaway, t_{TR}, which also represented the end time of safety venting, preceded the peak $dT_{cell}\ dt^{-1}$ value determined from the cell temperature trend. This peak $dT_{cell}\ dt^{-1}$ value often surpassed 100 K s^{-1}. The onset time of thermal runaway occurred shortly before the peak $dT_{cell}\ dt^{-1}$ value, and was defined as 0.5 s before $dT_{cell}\ dt^{-1}$ became greater than 14 K s^{-1}. 14 K s^{-1} was the minimum value that pinpointed the start of a sudden dramatic rise in temperature.

The safety venting and thermal runaway onset times were verified for every cell by comparing them to manually recorded times during experiments. Safety venting onsets were identified during experiments by a clear, audible clicking sound and the visual appearance of ejected gases exiting the wind tunnel exhaust elbow. Thermal runaway onsets were identified during experiments by a dramatic increase in the ejection rate coming from the exhaust elbow (and visible flame jetting in the air environment tests) and accompanying explosion sounds. After identifying and verifying t_{SV} and t_{TR}, the corresponding onset temperatures of safety venting and thermal runaway were also recorded.

The end time of thermal runaway, t_{ETR}, occurred shortly after the peak $dT_{cell}\ dt^{-1}$ value, and was defined as 0.5 s after $dT_{cell}\ dt^{-1}$ fell below 6.5 K s^{-1}. 6.5 K s^{-1} was the value that best pinpointed times corresponding to the times that the measured O_2 production from the failing cell ceased. This criterion was verified on cell #2 for each array tested in nitrogen, because cell #2 always failed first and was not accompanied by the failure of other cells; so any change in the measured O_2 signal was only contributed by the thermal runaway of cell #2. The end time of thermal runaway was not clearly identified during the experiments, but was estimated as the time that the ejection rate from the exhaust elbow decreased significantly to allow for further verification.

The onset of safety venting, onset of thermal runaway, and end of thermal runaway are all identified for a representative cell on the plot in Figure 3.1.

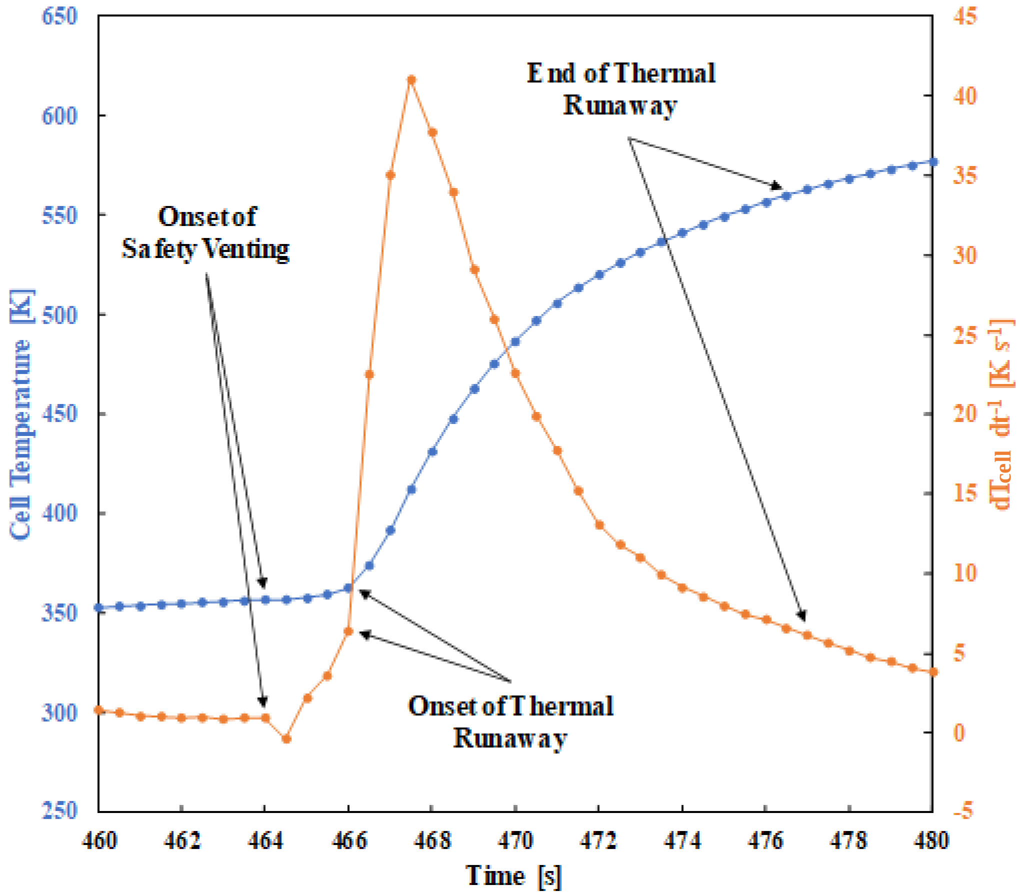

Figure 3.1: Onset of safety venting, onset of thermal runaway, and end of thermal runaway identified for a representative cell.

3.2 Cell Mass Loss Rates

Each cell tested was weighed before and after each experiment. These initial and final mass values were used to develop estimated time-resolved mass and mass loss rate trends for each cell. A major assumption in these estimations was that the mass was lost linearly (constant mass loss rate) [22-24, 26]. For the cells at 100% SOC, the onset of safety venting was often indistinguishable, so it was assumed that all of the mass loss occurred during the duration of thermal runaway. Previous studies indicate that approximately 15% of the mass loss at 100% SOC actually occurs during safety venting [23-24], but the lack of a clear safety venting stage for many cells and the lack of any discernable changes in the gas concentration trends before thermal runaway suggested that neglecting this was a reasonable assumption. For the cells at 50% SOC, however, the onset of safety venting was always identified. For these cells, it was assumed that 52% of the mass loss occurred during safety venting, and 48% occurred during thermal runaway. These percentages were assumed based upon mass loss data for identical cells published in previous studies [23-24, 26]. For each test, the mass loss rate trends for each cell were added together to determine the total mass loss rate of the cell array, $\dot{m}_{LIBs}$. An example of the developed mass and mass loss rate trends for a representative cell at 50% SOC is shown in Figure 3.2.

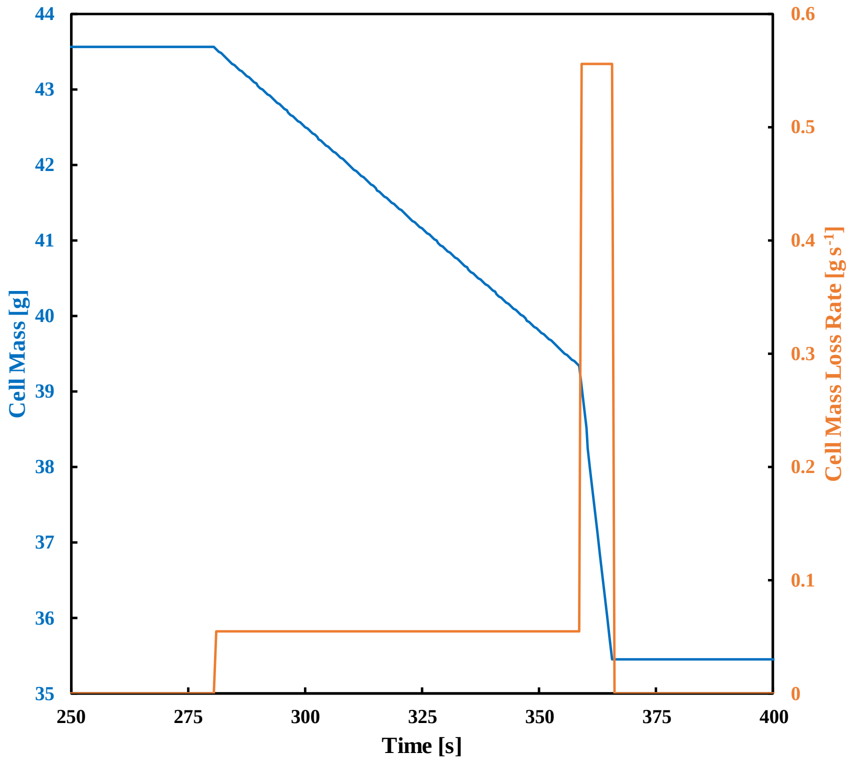

Figure 3.2: Developed mass loss and mass loss rate trends for a representative 50% SOC cell.

3.3 Concentrations, Yields, and Flammability Limits of Ejected Gases

Signals from the five gas sensors were used to estimate gas yields ejected from the cell arrangements in the nitrogen environment tests. Preliminary experiments were conducted to determine the gas transport time to each sensor and the response time of each sensor. Exact times varied based on the sensor, but all transport times varied between three and 7.5 seconds, and all response times varied between 1.5 and four seconds. These time delays were offset in the data analysis to align the gas signal peaks with the times of thermal runaway. Due to the inert, single gas atmosphere, all recorded gas signals were known to have been ejected from the cells themselves. Gas yields were not calculated for tests conducted in air for a number of reasons related to combustion. First, most flammable gases ejected from the cells, including THC, CO, and H_2, were consumed in the combustion process. Second, any oxygen ejected from the cells was indistinguishable due to the large oxygen consumption associated with the presence of a flame. Third, it was impossible to determine if any measured CO_2 was ejected from the cells or formed in the combustion process. Gas signals from an example nitrogen environment test are shown in Figure 3.3. The signals were originally measured as a voltage, but were converted to volumetric concentrations through gas cylinder calibration. Methane was assumed to be the dominant THC gas [36], so the THC sensor was calibrated against methane and the signal was considered to be methane for all calculations.

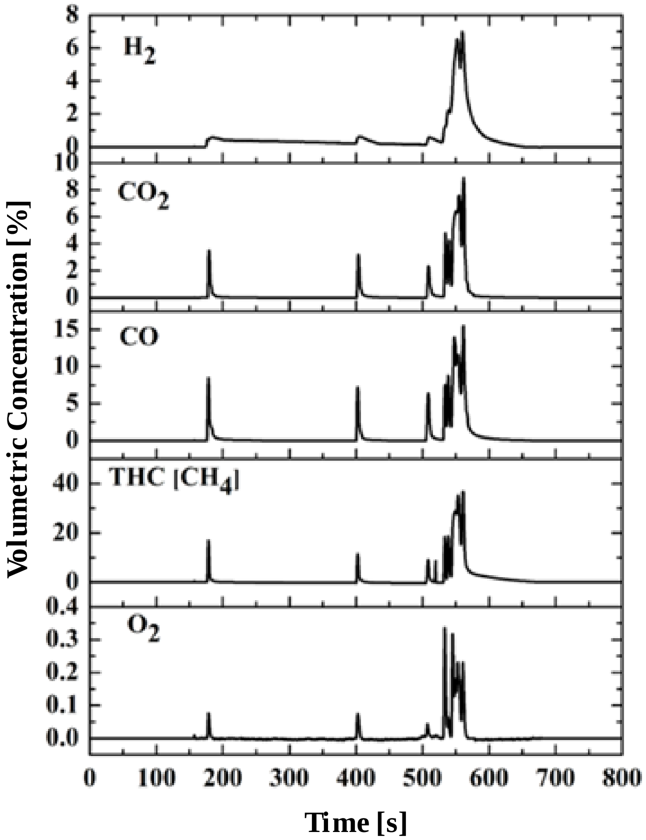

Figure 3.3: Example gas signals (shown as percentages of the total gas volume) plotted against time for a 12 cell, 100% SOC test in N_2 with no gaps.

Mass yields, m, for each of the measured gases, i, were determined by integrating the mass flow rates, $\dot{m}$, for each gas between t_{SV} and t_{ETR}. These mass flow rates were determined by equating the gas to nitrogen ratios for the mass flow rates and mass fractions, Y. The mass flow rate of nitrogen was set and measured by the mass flow controller, and mass fractions were calculated as functions of the measured mole fractions, X, and the corresponding molecular weights, M. The mole fraction of nitrogen was estimated by assuming that it made up the remainder of the gas stream not measured by the gas sensors. This process is shown in detail in Equations 3.1, 3.2, and 3.3.

$$m_i=\int_{t_{SV}}^{t_{ETR}} \dot{m}_i\,dt \tag{3.1}$$

$$\dot{m}_i=\frac{Y_i}{Y_{N_2}}\dot{m}_{N_2} \tag{3.2}$$

$$\frac{Y_i}{Y_{N_2}}=\frac{X_i M_i}{(1-\sum X_i)M_{N_2}} \tag{3.3}$$

The mass yields of the flammable gases (THC, CO, and H_2) were converted to moles, *n*, and used to calculate the lower flammability limit in air (*LFL*) of a mixture of the gases ejected from the cells. This calculation process, following Le Chatelier's mixing rule, is outlined in Equations 3.4, 3.5, and 3.6.

$$n_j=\frac{m_j}{M_j} \tag{3.4}$$

$$X_j=\frac{n_j}{\sum n_j} \tag{3.5}$$

$$LFL=\left[\sum\left(\frac{X_j}{LFL_j}\right)\right]^{-1} \tag{3.6}$$

In these equations, the subscript *j* only represented any of the flammable gases ejected from the cells, meaning the O_2 and CO_2 mass yields were neglected. Any possible suppressing effects of the produced CO_2 were ignored in this calculation in order to provide the most conservative LFL value. LFL values in air of 5%, 12.5%, and 4% by volume were assumed for THC, CO, and H_2, respectively [53]. Additionally, the maximum air volume that could achieve the LFL from the failure of a single cell was determined using the equation of state for ideal gases, assuming standard temperature and pressure conditions.

3.4 Energy Generation

3.4.1 Chemical Heat Generation (Nitrogen Tests)

The chemical heat generated from the reactions between cell components, E_{CHG}, was calculated for the nitrogen atmosphere tests. No combustion occurred in these tests, so the chemical reactions were the only source of energy generation. The sum of the five calculated gas mass yields (as described in the previous subsection) did not account for all of the mass lost by the cells, as there was a significant mass of particulate matter ejected from the cells as well. Therefore, the heat carried by the solid particulates was taken into account in the E_{CHG} calculation. E_{CHG} was calculated with Equation 3.7, integrated from the start of each test to the end of each test, t_{end}.

$$E_{CHG}=\int_0^{t_{end}} P_{CHG}\,dt=\int_0^{t_{end}}\left\{\left[\dot{m}_{N_2}\overline{c_p}_{N_2}+\sum\left(\dot{m}_i\overline{c_p}_i\right)+\dot{m}_C\overline{c_p}_C\right](T_{ex}-T_0)+P_{loss}-P_{heater}\right\}dt \quad (3.7)$$

This energy balance consists of five main terms constituting the rate of chemical heat generation, P_{CHG}: the heat carried by the nitrogen flow, the heat carried by the gases ejected from the cells, the heat carried by the solid particulates (approximated as graphite) ejected from the cells, the heat lost to the surroundings, and the heat inputted from the DC power supply.

The nitrogen, ejected gas, and graphite terms are expressed as functions of mass flow rate, average specific heat, $\overline{c_p}$, average reading of the three exhaust thermocouples, T_{ex}, and initial average reading of the three exhaust thermocouples, T_0, which represents the temperature of the system before the onset of failure processes. All specific heats were averaged over the interval of temperature increase with Equation 3.8.

$$\overline{c_p}=\frac{\int_{T_0}^{T_{ex}} c_p dT}{T_{ex}-T_0} \quad (3.8)$$

All specific heats used in Equation 3.8, c_p, were calculated with temperature dependent polynomial equations found in literature [54-55]. The nitrogen mass flow rate was set and measured by the mass flow controller and the measured gas mass flow rates were calculated identically to the mass yield analysis. The graphite mass flow rate was estimated by subtracting the sum of the measured gas mass flow rates from $\dot{m}_{LIBs}$, as shown in Equation 3.9.

$$\dot{m}_C=\dot{m}_{LIBs}-\sum\dot{m}_i \tag{3.9}$$

The power loss term, P_{loss}, accounted for the energy loss to the steel hexagonal struts of the cell holder and insulation in the test section. In all cases, this heat loss was assumed to be primarily conductive and was calculated according to Fourier's law (approximating the spatial temperature derivative with a finite temperature difference), as shown in Equation 3.10.

$$P_{loss}=kA\frac{T_{ex}-T_0}{L} \tag{3.10}$$

For calculating P_{loss}, the average exhaust temperature was smoothed using a second order Savitzky-Golay filter. This filter was necessary to account for thermal inertia of the solid elements that conducted heat away from the test section. The Savitzky-Golay filter was selected in particular due to its applicability to transient processes. P_{loss} also depended on the material thermal conductivity, k, which was calculated at average temperatures using polynomial equations found in literature [50, 56], the material surface area to which heat was lost, A, and the material length/thickness through which heat was conducted, L. Area and length values for the top insulation, side and bottom insulation, and hexagonal struts are shown in Table 3.1.

Table 3.1: Areas and lengths / thicknesses used in the power loss estimation.

	***A* [m²]**	***L* [m]**
Top insulation	3.6E-2	1.905E-2
Side and bottom insulation	9.54E-2	6.35E-3
Steel hexagonal struts	2.22E-4	1E-2

The input power trend, P_{heater}, was developed by monitoring the DC power supply during experiments. P_{heater} would initially be set to approximately 110 W. This power was attempted to be maintained throughout each experiment, but the violent nature of the LIB failure often caused the heating wire to break or short, resulting in a decrease in input power (most of the time decreasing all the way to zero). While the input power was not always completely user-controlled, it was always monitored, so P_{heater} trends were able to be developed. On average, the integral of P_{heater} was 39.3 ± 10.9 kJ for a given test. The energy inputted by the heater was minor relative to the energy generated by the cells. At most, the input energy was only 10% as much as E_{CHG}, so its variation from test-to-test had little impact on the overall failure dynamics and energetics.

Figure 3.4 presents P_{CHG} data from an example test. From the figure, it can be seen that no energy was generated before thermal runaway, sharp peaks developed during failure, and energy generation slowly decayed as the cells cooled down. Additionally, it is clear from the figure that the input power (110 W) was minimal compared to the power generation.

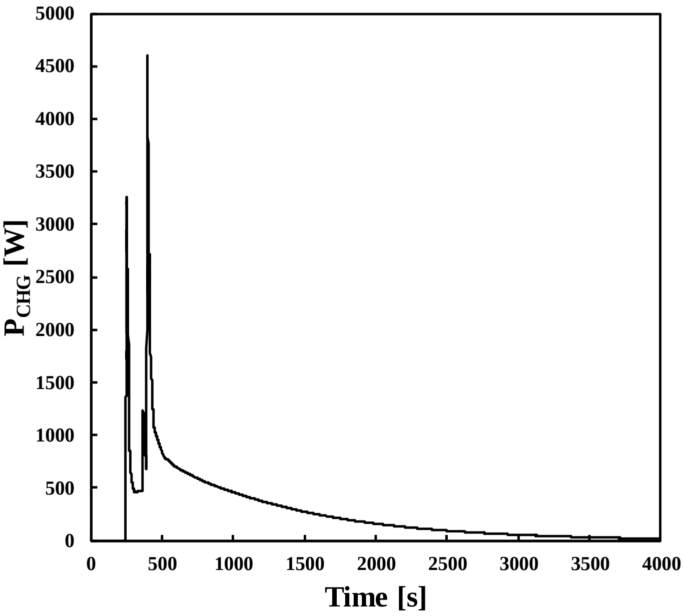

Figure 3.4: P_{CHG} trend from a 15 cell, 100% SOC test in N_2 with 5 mm gaps.

3.4.2 Flaming Combustion Energy (Air Tests)

In the air atmosphere tests, flaming combustion energy, E_{flame}, was estimated rather than chemical heat generation. E_{flame} was estimated based on oxygen consumption methodology, as shown in Equation 3.11.

$$E_{flame} = \int_0^{t_{end}} \left(\dot{m}_{O_2} - \dot{m}_{O_{2_0}}\right) \Delta H_c^{O_2}\, dt \tag{3.11}$$

In this equation, the initial oxygen mass flow rate, $\dot{m}_{O_{2_0}}$, was set and measured by the mass flow controller, and $\dot{m}_{O_2}$ was calculated using the same methodology outlined in section 3.3. The heat of combustion per gram of oxygen consumed, $\Delta H_c^{O_2}$, was assumed constant at 13.1 kJ g^{-1} [29], although it is acknowledged that this value drops when CO is produced in large quantities.

Unfortunately, E_{flame} was underestimated due to incomplete combustion inside the wind tunnel. The high burning rate achieved in the experiments made it impossible to supply enough air to provide a well-ventilated environment throughout the duration of failure (this may simulate more realistic conditions inside battery packs, however). Despite the high flow rate (640 L min^{-1}), the oxygen concentration often dropped below 5 vol. % when many cells failed simultaneously. There were also significant spikes in the THC and CO trends during these time periods, indicating that many flammable ejected gases did not combust. Figure 3.5 shows gas trends from an example air atmosphere test.

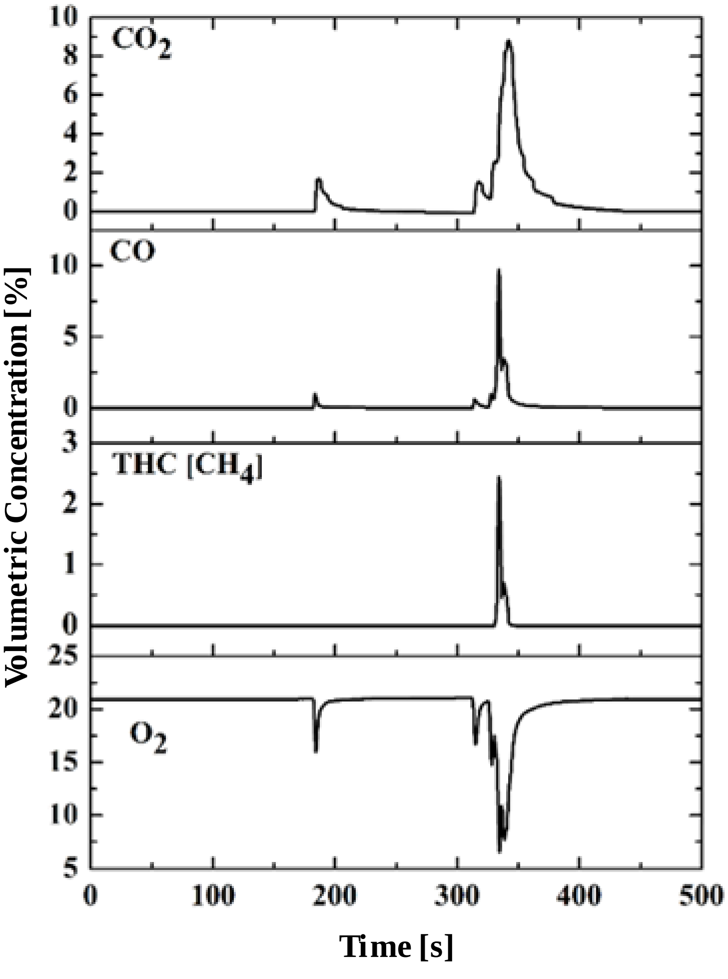

Figure 3.5: Example gas signals (shown as percentages of the total gas volume) plotted against time for a 12 cell, 100% SOC test in air.

To determine E_{flame} values for nearly complete combustion, the CSBC / cone calorimeter tests were conducted on single cells. The heat release rate trends outputted by the cone calorimeter were integrated over the entire spans of the tests to calculate E_{flame}. The E_{flame} values obtained from the wind tunnel experiments were normalized per cell to provide a direct comparison to the CSBC / cone calorimeter results. Representative example trends of the integrand on the right side of Equation 3.11 and the heat release rate curves outputted by the cone calorimeter, both labeled P_{flame}, are plotted against time in Figure 3.6.

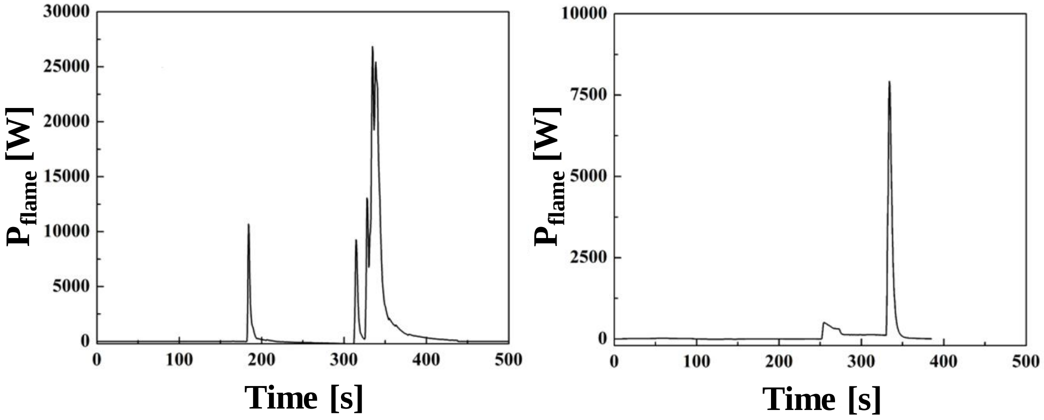

Figure 3.6: P_{flame} trends from representative air tests, from a 12 cell array in the wind tunnel (left) and a single cell in the CSBC / cone calorimeter (right). The sharp peaks correspond to cells undergoing thermal runaway.

Chapter 4: Results and Discussion

4.1 Cascading Failure Dynamics

Diagrams tracking the propagation of thermal runaway through an array are shown in Figures 4.1 and 4.2. The failure propagation diagrams from one test of each type are shown. The physical spacing between the cell array images in the diagrams is meant to give a qualitative (not drawn to scale) understanding of the timespan between subsequent cell failures.

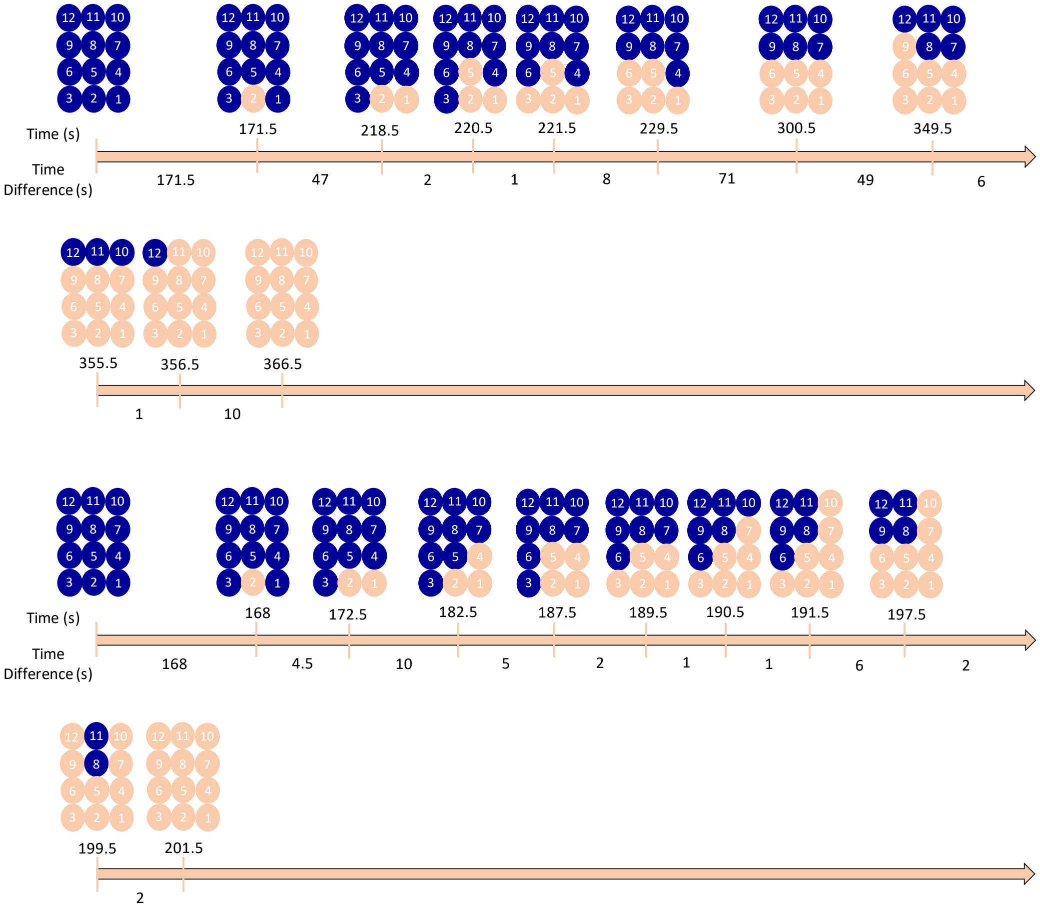

Figure 4.1: Thermal runaway propagation diagrams for example tests from the 12 cell, 100% SOC tests in N_2 (top two rows) and air (bottom two rows). Dark circles represent sound cells and light circles represent cells that have underwent thermal runaway.

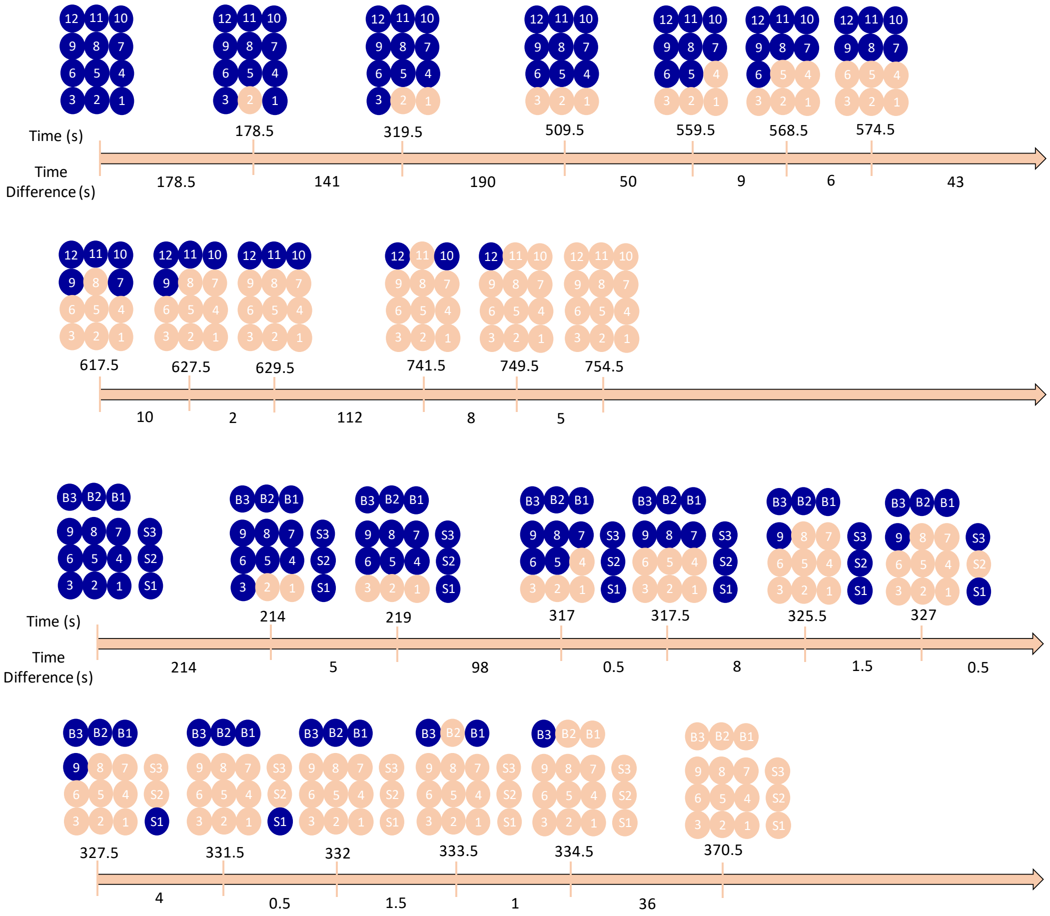

Figure 4.2: Thermal runaway propagation diagrams for example tests from the 12 cell, 50% SOC tests in N_2 (top two rows) and 15 cell, 5 mm gap tests in N_2 (bottom two rows). Dark circles represent sound cells and light circles represent cells that have underwent thermal runaway.

All cells underwent thermal runaway in nearly every test conducted. Test 3 in the 12 cell, 100% SOC in N_2 set and test 4 in the 12 cell, 50% SOC in N_2 set each had one cell that did not reach thermal runaway, but these were likely due to the fact that the cells became dislodged from their original positions during the tests. Despite mitigation efforts of lowering SOC and instituting gaps between cells, failure propagation was unable to be ceased.

Apart from a few exceptions, a cell generally underwent thermal runaway after at least one cell directly adjacent to it already had. This was expected, as the dramatic temperature rise from a failing cell undoubtedly subjected the surrounding cells to greater incoming heat fluxes (particularly conductive heat fluxes). Additionally, most tests generally propagated on a row-to-row basis, meaning all of the cells in row 1 failed before all of the cells in row 2, and so on. The failure propagation dynamics of each test of the same type were similar, but the timing of failure of individual cells varied considerably from test-to-test, despite the carefully controlled conditions.

By averaging the thermal runaway times of all three cells in each row, the thermal runaway propagation speed from row-to-row was calculated. These propagation speeds are plotted for each row-to-row jump in each test configuration in Figure 4.3. It should be noted that this plot neglects the detached side column in the 5 mm gap tests, to provide the most direct comparison. Additionally, the average row-to-row propagation speed across all rows for each test configuration is shown in Table 4.1. The error bars in Figure 4.3 and uncertainty in Table 4.1, along with all other error bars and uncertainties in this thesis, were calculated from the scatter in the data as two standard deviations of the mean.

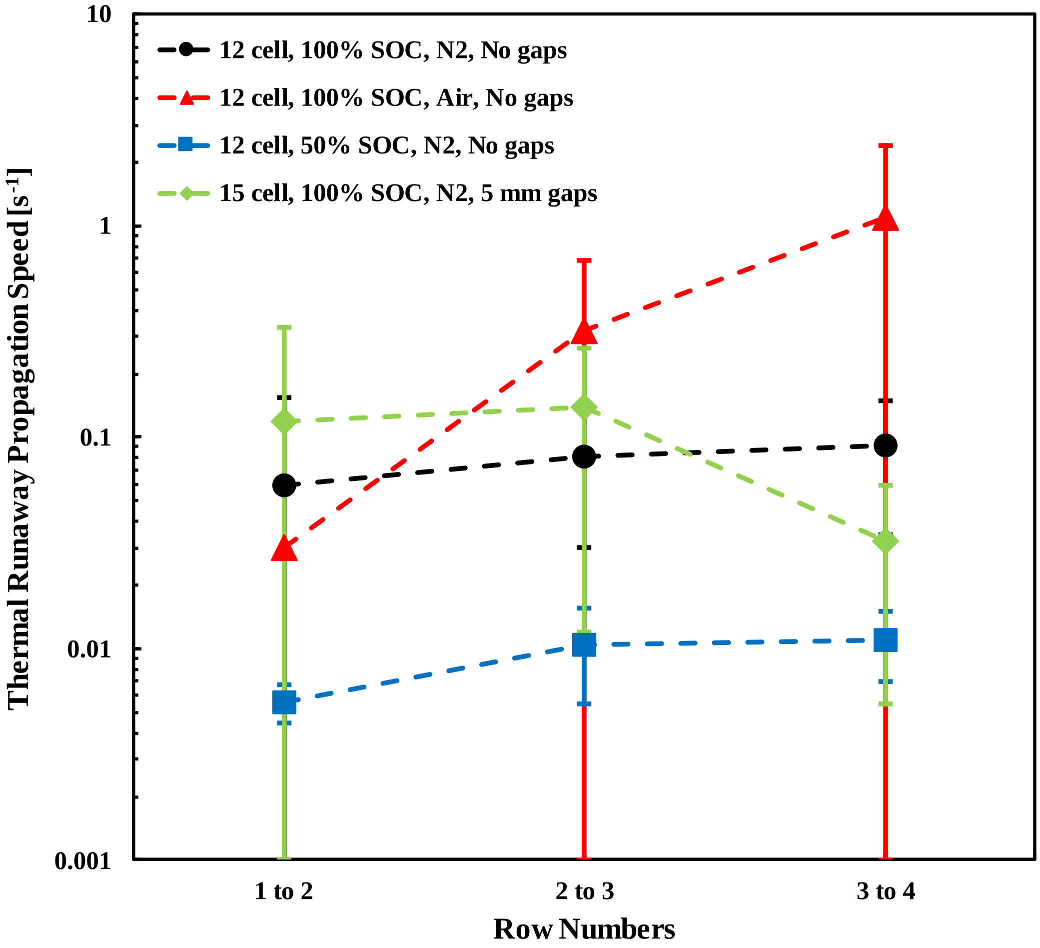

Figure 4.3: Average thermal runaway propagation speeds for each row-to-row propagation in each test configuration. Speeds are plotted on a logarithmic (base 10) scale.

Table 4.1: Average row-to-row thermal runaway propagation speed across all rows for each test configuration.

Test configuration	**Average Row-to-Row Thermal Runaway Propagation Speed [s^{-1}]**
12 cell, 100% SOC, N_2, No gaps	0.077 ± 0.038
12 cell, 100% SOC, Air, No gaps	0.48 ± 0.49
12 cell, 50% SOC, N_2, No gaps	0.0091 ± 0.0025
15 cell, 100% SOC, N_2, 5 mm gaps	0.096 ± 0.079

As shown, the tests conducted in air propagated on average approximately 7.5 times faster than the equivalent tests conducted in nitrogen. This was associated with the presence of a flame during thermal runaway, which provided additional heating to the adjacent cells, causing them to fail earlier. Placing the cells in a nitrogen environment removed this heat source and slowed down the propagation. Interestingly, the average propagation speed from row 1 to row 2 in the air tests was actually less than the equivalent tests in nitrogen. This was likely due to the higher flow rate in air which provided a higher cooling rate; the impact of the higher cooling rate was diminished by the developing fire for later row propagations, however. While the average propagation speed in air was considerably faster than it was in nitrogen, there are very large uncertainties associated with the measurements. In many tests, especially those conducted in air, the propagation occurred quickly enough that a difference in failure time of half a second caused a significant shift in the propagation speed. Additionally, the thermocouples were only reading at a maximum of 2 Hz, so any propagation occurring faster than that was not captured. Due to this uncertainty, the air results for each row-to-row jump are best compared qualitatively rather than quantitatively.

When viewed on an average basis across all of the rows, as shown in Table 4.1, the uncertainty for the speed in the air tests was greater than ± 100%. From Figure 4.3, it is clear that the speed for the air tests was not constant, but instead appeared to accelerate as the thermal runaway propagation progressed through the cell array. More tests are necessary to confirm this behavior, but fitting the current data linearly provides a constant row-to-row thermal runaway acceleration of 0.54 s^{-1} per thermal runaway row propagation. Additional tests with additional rows of cells would prove whether this acceleration is actually continuous or not.

While decreasing the SOC to 50% did not stop the failure propagation altogether, it did slow the propagation considerably. On average, the tests conducted at 50% SOC propagated approximately 8.5 times slower that the equivalent tests conducted at 100% SOC. The uncertainties for these tests were smaller due to the longer timescales, so the speed measurements can be compared more quantitatively. The slower propagation speeds can be attributed to reduced chemical energy release (associated with the reduced SOC) [20-26], which in turn leads to lower temperatures reached during failure (discussed in the next subsection).

The presence of a 5 mm gap was not able to prevent thermal runaway propagation altogether, but it did appear to have some impact on the propagation speed. The uncertainties are large, but on average the propagation speed was about four times slower between rows 3 and 4 (where the gap was located) than it was between earlier rows in the 5 mm gap tests. Additionally, the average propagation speeds from rows 1-3 and 3-4 in the 5 mm gap tests were about two times faster and three times slower, respectively, than they were in the 100% SOC tests in N_2 without any gaps. The faster propagation speed through the earlier rows was likely due to the lack of conduction to the fourth row. The large uncertainties make these findings rather inconclusive, however.

4.1.1 5 mm Gap Analysis

Multiple analyses were conducted in an effort to determine how the 5 mm gap impacted the heat transfer between rows 3 and 4. First, the row 4 cell temperatures were determined right before the first row 3 thermal runaway time, for 100% SOC N_2 tests with and without the 5 mm gap. With the 5 mm gap, the average row 4 temperature was 308 ± 6 K, and without it, the average row 4 temperature was 319 ± 7 K. The presence of the gap primarily impacted the conductive heat transfer before thermal runaway occurred. These two temperatures are within each other's uncertainties, but assuming a typical initial temperature of 295 K, the increase in row 4 temperature for the 5 mm gap tests was only about 56% as much as the tests without gaps, during the pre-row 3 thermal runaway time period. Similarly, the average $dT_{cell}\ dt^{-1}$ values for each row 4 cell were taken for the 50 seconds prior to the first row 3 thermal runaway in each test. Average heating rates of 0.16 ± 0.10 and 0.24 ± 0.06 K s^{-1} were determined for the tests with and without the 5 mm gap, respectively. The presence of the 5 mm gap resulted in about a 33% slower heating rate to row 4, when compared to the heating rate without the gap. Both the temperature and $dT_{cell}\ dt^{-1}$ analyses indicate that the fourth row cells in the 5 mm gap tests are still heated by convection and radiation despite the absence of direct conduction. Based on the $dT_{cell}\ dt^{-1}$ analysis results, conduction contributed to about one third of the overall heating to the fourth row.

Additionally, the average $dT_{cell}\ dt^{-1}$ values for each row 4 cell were taken between the first row 3 thermal runaway time and the thermal runaway time of the row 4 cell of interest. During this time period, average heating rates of 1.4 ± 0.4 and 1.8 ± 0.4 K s^{-1} were determined for the tests with and without the 5 mm gap, respectively (meaning the heating rate to row 4 with the 5 mm gap was roughly 25% slower than it was without the 5 mm gap). The row 3 temperatures increased rapidly during this time period, and the heat transfer to row 4 became complex. Forced flow through the 5 mm gap potentially increased the convective heat transfer, but the greater overall heating rate without the gap indicated that radiation likely dominated during this post-row 3 thermal runaway time period, with convection not playing as significant a role.

In general, all analyses on the impact of the 5 mm gap concluded that the gap prevented conductive heat transfer and slowed the thermal runaway propagation to some degree. Ultimately, however, all of the determined temperatures and heating rates were within each other's uncertainties with and without the 5 mm gap, and most importantly, the propagation of thermal runaway was never prevented. The lack of conduction to the fourth row with the 5 mm gap was not particularly impactful because, based on the $dT_{cell}\ dt^{-1}$ analyses, conduction only contributed about one third of the overall heating before thermal runaway of row 3 and about one fourth of the overall heating after thermal runaway of row 3. From a failure mitigation point of view, the 5 mm gap was not very impactful.

4.2 Onset and Maximum Temperatures

The temperatures measured at the onset times of safety venting and thermal runaway were recorded for each cell. While the failure onset times varied from cell-to-cell due to their differing positions, the failure onset temperatures were fairly consistent for all cells. No discernable trend was identified for the failure onset temperatures on a cell, row, or column basis; therefore, all failure onset temperatures for all cells tested in each test configuration were averaged together and are reported in Table 4.2. Table 4.2 also reports the average maximum temperature for all cells in each test configuration. For most cells, the maximum temperature occurred soon after the end of thermal runaway, however, for some cells, the maximum temperature occurred long after thermal runaway due to heat being transferred from an adjacent failing cell.

Table 4.2: Average safety venting onset, thermal runaway onset, and maximum cell temperatures for each test configuration. Temperatures are measured at the bottom surface of each cell.

Test configuration	Safety venting onset temperature [K]	Thermal runaway onset temperature [K]	Maximum cell temperature [K]
12 cell, 100% SOC, N_2, No gaps	359 ± 17	381 ± 12	686 ± 23
12 cell, 100% SOC, Air, No gaps	350 ± 16	371 ± 11	727 ± 33
12 cell, 50% SOC, N_2, No gaps	406 ± 12	452 ± 14	638 ± 20
15 cell, 100% SOC, N_2, 5 mm gaps	351 ± 9	383 ± 10	683 ± 26

As shown, the cells tested in N_2 at 100% SOC showed extremely similar onset and maximum temperatures with and without the 5 mm gaps. The average onset temperatures were lowest and the average maximum temperature was greatest for the tests conducted in air. The failure onset temperatures in air were only about 10 K less than the temperatures for 100% SOC cells tested in N_2, but the maximum temperatures were upwards of 40 K greater. This can likely be explained by the fast, intense heating from the flame and rapid propagation of failure from cell-to-cell. Additionally, the tests conducted at 50% SOC showed the greatest onset temperatures and the lowest maximum temperatures, likely due to the lesser released chemical energy (which correlates with the stored energy) [20-26]. These values differed significantly from cells tested at 100% SOC in N_2, with the average safety venting onset temperature, thermal runaway onset temperature, and maximum temperature being about 50 K greater, 70 K greater, and 50 K less, respectively.

It is also important to note that the temperatures reported here were measured at the bottom surface of the cells only. Preliminary tests were conducted to determine if the temperature was uniform throughout the cell by placing thermocouples at the mid-height of the cell sidewall as well as the bottom surface. Throughout the tests, the sidewall thermocouples measured higher temperatures than the bottom surface thermocouples, especially during thermal runaway, when the sidewall thermocouples often measured peak temperatures over 300 K higher. Therefore, the temperatures presented in Table 4.2 apply strictly to the bottom surface of the cell only, and should not be applied more globally to the cell as a whole, due to significant spatial non-uniformity.

Previously reported failure onset and maximum temperatures vary from the results reported here. Liu et al. [23-24] reported safety venting onset temperatures, thermal runaway onset temperatures, and maximum temperatures of 470 ± 4, 500 ± 2, and 698 ± 6 K, respectively, for cells at 50% SOC, and 451 ± 5, 470 ± 4, and 701 ± 20 K, respectively, for cells at 100% SOC. Their temperatures (with the exception of the 100% SOC maximum temperature) are all significantly greater than the temperatures reported here due to the differences in cell heating. Liu et al. heated their tested cells slowly (20 W) and uniformly inside of a copper slug. In the current experiments, the heating was much faster and more non-uniform, as the majority of the heating was incoming from one side of the cells. The bottom of the cell casing is separated slightly from the reacting components of the cell, so the bottom surface temperature is lower than most other locations along the cell casing. This highlights the impact that heating scenario has on onset of cell failure. Temperature-based failure detection thresholds for real battery packs should not be based on experiments with slow, uniform heating rates because the temperatures of the cells are often not spatially uniform in real failure scenarios. By measuring the temperatures of the bottom surfaces of the cells with fast, non-uniform heating rates, the current measurements provide more conservative failure onset temperatures that should be used in real battery packs.

It also should be noted that the current tests conducted in air actually resulted in slightly higher maximum temperatures than those reported by Liu et al. The small wind tunnel cross section, forced air flow, and presence of multiple failing cells in the current tests lead to more direct flame impingement on the cells than in the CSBC tests, likely resulting in the greater average maximum cell temperature.

4.3 Mass Loss and Ruptured Cells

The total mass loss of each cell was determined by weighing them before and after each experiment. This mass loss was fairly constant for each cell within a particular test; the cell's position within the array did not appear to have an effect on its mass loss. Cells that did lose more mass than average tended to be cells that ruptured. The steel casing of these cells cracked and many of the solid interior components were ejected. The position of a cell within an array did not appear to influence its probability of rupture. Figure 4.4 provides a visual comparison of a failed ruptured cell versus a cell that failed but did not rupture.

Figure 4.4: Photograph of a failed ruptured cell (bottom right) compared with a failed non-ruptured cell (top left).

Table 4.3 provides the total number of ruptured cells for each experiment conducted, along with an average for each test configuration and the percentage of the total number of cells in the array that the average represents. Table 4.4 provides the average mass loss per cell for each test configuration and the corresponding percentages of the average cell initial mass (43.57 ± 0.03 g) that was lost.

Table 4.3: Total number of ruptured cells for all experiments.

Test configuration	Test number	Number of ruptured cells
12 cell, 100% SOC, N_2, No gaps	1	1
	2	2
	3	2
	4	2
	Average	1.75 (14.6%)
12 cell, 100% SOC, Air, No gaps	1	3
	2	2
	3	4
	4	2
	Average	2.75 (22.9%)
12 cell, 50% SOC, N_2, No gaps	1	0
	2	0
	3	0
	4	1
	Average	0.25 (2.1%)
15 cell, 100% SOC, N_2, 5 mm gaps	1	2
	2	2
	3	1
	4	2
	Average	1.75 (11.7%)

Table 4.4: Average cell mass loss and the corresponding percentage of the average initial cell mass that was lost for each test configuration.

Test configuration	**Failed cell mass loss [g]**	**Percentage of average initial cell mass that was lost [%]**
12 cell, 100% SOC, N_2, No gaps	16.7 ± 1.0	38.4 ± 2.3
12 cell, 100% SOC, Air, No gaps	18.1 ± 1.5	41.5 ± 3.4
12 cell, 50% SOC, N_2, No gaps	8.4 ± 0.6	19.2 ± 1.3
15 cell, 100% SOC, N_2, 5 mm gaps	16.5 ± 1.1	37.9 ± 2.4

As shown, the average mass loss was greatest for the tests in air, but it was still within the uncertainty of the 100% SOC N_2 tests. This small increase in average mass loss can be attributed to the higher test section temperatures and slightly greater number of ruptured cells occurring in the air tests. Additionally, the 100% SOC N_2 tests showed very similar mass loss and number of ruptured cells with and without the 5 mm gaps. Most significantly, however, the tests conducted at 50% SOC showed approximately 50% less mass loss than the equivalent tests conducted at 100% SOC. This reduced mass loss, along with the almost nonexistent presence of ruptured cells (only one cell ruptured in all four tests conducted), can be attributed to the lower stored electrical energy and released chemical energy [20-26], which, in turn, led to the slower ejection of mass and less frequent rupture.

Liu et al. [23-24] reported mass loss of 6.7 ± 0.3 g at 50% SOC and 16.0 ± 1.3 g at 100% SOC from CSBC experiments on identical LCO cells. Quintiere et al. [25] reported mass loss of approximately 7.2 g for 50% SOC cells and 15.0 g for 100% SOC cells from similar experiments. These compare relatively well with the results reported here, but the slightly larger values from the current tests can once again be attributed to rupturing cells, which did not occur in the previous investigations because the cell sidewalls were contained by a copper slug.

4.4 Gas Yields and Flammability Limits

Signals from the gas sensors were used to calculate O_2, THC, CO, CO_2, and H_2 mass yields for each test conducted in nitrogen. The yields are presented per failed cell and per unit initial mass of a failed cell in Table 4.5.

Table 4.5: Average gas species mass yields for each measured gas for each test configuration.

Test configuration	Gas	Species yield per failed cell [g]	Species yield per unit initial cell mass [-]
12 cell, 100% SOC, N_2, No gaps	**O_2**	0.023 ± 0.006	0.0005 ± 0.0001
	THC	1.53 ± 0.83	0.035 ± 0.019
	CO	1.64 ± 0.38	0.038 ± 0.009
	CO_2	1.27 ± 0.26	0.029 ± 0.006
	H_2	0.084 ± 0.016	0.0019 ± 0.0004
12 cell, 50% SOC, N_2, No gaps	**O_2**	< 0.006	< 0.0001
	THC	0.51 ± 0.32	0.012 ± 0.007
	CO	0.18 ± 0.02	0.004 ± 0.001
	CO_2	0.32 ± 0.04	0.007 ± 0.001
	H_2	0.030 ± 0.006	0.0007 ± 0.0001
15 cell, 100% SOC, N_2, 5 mm gaps	**O_2**	0.019 ± 0.002	0.0004 ± 0.0001
	THC	2.94 ± 0.30	0.067 ± 0.007
	CO	2.40 ± 0.25	0.055 ± 0.006
	CO_2	1.84 ± 0.12	0.042 ± 0.003
	H_2	0.118 ± 0.011	0.0027 ± 0.0003

On a mass basis, THC, CO, and CO_2 (to a lesser degree) were the dominant gases produced. The large CO production, in particular, provided a significant chemical hazard due to its natural toxicity. Hydrogen production, while less than other gases, was also significant. Additionally, while very small, oxygen production was observed in the gas trends corresponding to the times of thermal runaway. Oxygen mass yields were calculated for all 100% SOC tests. At 50% SOC, the oxygen peaks were often indistinguishable from the noise in the trend, so only a maximum value was able to be estimated (hence the lack of uncertainty values for O_2 at 50% SOC in Table 4.5).

As shown, the species yields for the cells at 50% SOC were significantly less per cell than they were at 100% SOC, especially the CO yield. Despite the overall mass loss at 50% SOC being about half of the overall mass loss at 100% SOC, the gas yields at 50% SOC were significantly less than half of the gas yields at 100% SOC. The gas yields were also slightly greater for the 5 mm gap tests at 100% SOC than they were for the 100% SOC tests with no gaps. One possible explanation for this is greater overall test section temperatures and longer overall failure durations in the 5 mm gap tests, due to the greater thermal mass and number of cells; the prolonged higher temperatures promoted chemical reactions between cell components and the decomposition of cell components to a gaseous form.

Lyon and Walters [20-21] reported total volatile mass production from the failure of a single identical LCO cell of 0.95 and 4.46 g for cells at 43% and 100% SOC, respectively. These compare relatively well with the current results, with mass production of the five measured gases adding up to 1.08 ± 0.31 and 5.93 ± 1.27 g per failed cell at 50% and 100% (including data from tests both with and without 5 mm gaps) SOC, respectively. The small variance between the current results and the results of Lyon and Walters can be attributed to major differences in the methods of mass production determination. Lyon and Walters did not utilize gas sensors or calculate individual species yields. Instead, they measured mass production directly by weighing their test pressure vessel before and after venting the volatiles produced.

The yields of the flammable gases measured were converted to moles and used to calculate the lower flammability limit in air of the flammable gas ejected by the cells. Additionally, the moles of flammable gases produced and LFL were both used to calculate the maximum air volume that could achieve the lower flammability limit from a failed cell. This quantity combines the LFL and total volume of the mixture to provide a direct comparison of the flammability of the products ejected from a cell for each test configuration. These results are reported in Table 4.6.

Table 4.6: Average lower flammability limit (LFL) in air and maximum air volumes that could achieve the LFL from a failed cell.

Test configuration	**LFL in air [vol. %]**	**Maximum air volume that could achieve the LFL from a failed cell [m^3]**
12 cell, 100% SOC, N_2, No gaps	5.7 ± 0.1	0.085 ± 0.032
12 cell, 50% SOC, N_2, No gaps	4.9 ± 0.1	0.026 ± 0.010
15 cell, 100% SOC, N_2, 5 mm gaps	5.6 ± 0.1	0.142 ± 0.014

The lower flammability limit in air was nearly 1% less for the cells at 50% SOC than for the cells at 100% SOC, due to the fact that the mole fraction of hydrogen gas was greater for the 50% SOC tests than it was for the 100% SOC tests (only considering the flammable gases produced). Hydrogen gas has an LFL of 4 vol. %, and due to its large volume per unit mass, small fluctuations in the mass of hydrogen produced greatly affect the hydrogen mole fraction of the flammable gas stream, thus bringing the LFL closer to 4%. Similarly, for most test configurations the mass yields of THC and CO were fairly similar, yet the average LFLs were much closer to the LFL of THC (5%) than CO (12.5%) because the volume per unit mass of THC is significantly larger than CO.

Maloney [36] calculated LFL values for similar cells at various SOCs using a similar method. He calculated LFLs of about 7.5 and 9 vol. % in air for cells at 50% and 100% SOC, respectively. Maloney's values are greater than the values reported here because he measured CO concentrations of over 30 vol. % in his experiments, which were significantly greater than the current results. This increased CO concentration increased his calculated LFL.

The values for the maximum air volume that could achieve the LFL from a failed cell varied between test configurations primarily due to the differences in flammable gas production. The 5 mm gap tests produced the greatest mass of flammable gases, which corresponded to the greatest air volume in which the gases could still be ignited. Similarly, the 50% SOC tests produced the smallest mass of flammable gases, and subsequently the smallest air volume, even though the produced gases had the lowest LFL.

4.5 Energy Generation

4.5.1 Chemical Heat Generation (Nitrogen Tests)

The heat generated from the chemical reactions between cell components was calculated for all tests conducted in nitrogen. Those heat values are reported in Table 4.7 as the average heat per failed cell, per unit initial mass of a failed cell, and per unit initial stored electrical energy of a failed cell for each test configuration.

Table 4.7: Average chemical heat generation for each test configuration.

Test configuration	**Heat generated per failed cell [kJ]**	**Heat generated per unit initial cell mass [kJ g^{-1}]**	**Heat generated per unit initial stored electrical energy [-]**
12 cell, 100% SOC, N_2, No gaps	55.3 ± 1.4	1.27 ± 0.03	1.69 ± 0.05
12 cell, 50% SOC, N_2, No gaps	36.1 ± 1.6	0.83 ± 0.04	2.33 ± 0.07
15 cell, 100% SOC, N_2, 5 mm gaps	62.3 ± 3.5	1.43 ± 0.08	1.78 ± 0.09

On a per cell basis, the heat generated by 100% SOC cells in N_2 did not show significant dependence on whether the gaps were present; the average generated heats with and without the gaps are nearly within each other’s uncertainties. The value was slightly greater for the 5 mm gap tests, but this can likely be explained by the greater test section temperatures and longer overall failure duration due to the greater number of cells. The tests at 50% SOC actually generated roughly 65% as much energy as the 12 cell tests at 100% SOC. This resulted in the heat generation at 50% SOC being about 38% greater than at 100% SOC when normalized per unit stored electrical energy. Tests at additional SOCs would be required to confirm, but this indicates that chemical heat generation does not scale completely proportionally with SOC or stored electrical energy, even when only considering identical cells. Moreover, for all test configurations, the ratio between the chemical heat generation and the stored electrical energy was notably larger than 1, indicating that there is considerably more chemical energy stored in the cell that just what is stored during the discharge cycle.

The values normalized per failed cell compare well with values reported by Lyon and Walters [20-21]. They reported a chemical heat generation value of 65.7 kJ for a failed 100% SOC LCO cell. No value is directly reported for 50% SOC cells, but a reported fitted equation for chemical heat generation based on stored electrical energy would provide an average chemical heat generation value of 35.4 kJ. Liu et al. [23-24] reported chemical heat generation values of 37.4 ± 1.1 and 37.3 ± 3.3 kJ for LCO cells at 50% and 100% SOC, respectively. The current results compare well with their results at 50% SOC, but significantly overestimate their results at 100% SOC. Their setup, however, was designed to ignore the energy generated from reacting cell components after they had been ejected from the cell. This affected their 100% SOC results most significantly because those cells lost a much larger percentage of their mass than cells at lower SOCs. They provided an extrapolation to determine the chemical heat generation if no mass was lost (and all reactions occurred inside of the cell itself), and reported a value of 59.0 kJ, which compares well with the values reported here.

4.5.2 Flaming Combustion Energy (Air Tests)

Flaming combustion energy was calculated for the wind tunnel tests conducted in air as well as the CSBC / cone calorimeter tests. The results for flaming combustion energy normalized per failed cell, per unit initial mass of a failed cell, and per unit initial stored electrical energy of a failed cell, are reported in Table 4.8.

Table 4.8: Average flaming combustion energy for the wind tunnel tests in air and the CSBC / cone calorimeter tests.

Test configuration	Flaming combustion energy per failed cell [kJ]	Flaming combustion energy per unit initial cell mass [kJ g^{-1}]	Flaming combustion energy per unit initial stored electrical energy [-]
12 cell, 100% SOC, Air, No gaps	62.8 ± 18.4	1.4 ± 0.4	1.85 ± 0.55
CSBC / cone calorimeter	107.0 ± 17.7	2.5 ± 0.4	3.35 ± 0.57

As shown, the cell array tests only achieved 59% as much flaming combustion energy as the CSBC / cone calorimeter tests. As discussed in section 3.4.2, this is a result of significant incomplete combustion in the cell array tests. Once many cells began to fail in a timespan of only a few seconds, the oxygen inside the wind tunnel was mostly consumed, creating under-ventilated conditions. As a result, many flammable gases that were produced, such as THC and CO, were not fully combusted. It should be noted, however, that even with under-ventilated conditions, the flaming combustion energy was similar in magnitude to the chemical energy released and nearly two times the stored electrical energy of the cells. With near complete combustion, the ratio between the flaming combustion energy and stored electrical energy increased to a factor greater than three, and when also considering the heat generated from the cell chemical reactions, it increased to nearly a factor of five. During failure, these cells produce approximately five times more energy than what they store under normal operating conditions.

Liu et al. [23-24] reported a flaming combustion energy of only 48.7 ± 7.4 kJ for the same LCO cells at 100% SOC, but as discussed in section 2.3, they suffered issues related to incomplete combustion due to the violent, high-speed ejection rates of the cells. The addition of the collector / burner to the CSBC apparatus resulted in a nearly 60 kJ increase in flaming combustion energy, compared to their experiments. Quintiere et al. [25] conducted cone calorimeter tests on similar cells with a modified sample holder to help keep the cell in place during failure. They reported a flaming combustion energy per failed cell of about 60 kJ and a heat of combustion normalized by the cell initial mass of about 1.5 kJ g^{-1}. This coincidentally compares well with the wind tunnel test results presented here, but it was acknowledged that these results were impacted by incomplete combustion as well.

Chapter 5: Conclusions and Future Work

5.1 Conclusions

A new experimental facility was developed to provide detailed analysis of dynamics, ejected gases, and energetics relating to cascading failure in small scale LIB cell arrays. Four different test configurations with well-defined boundary conditions were studied to provide baseline data on cascading failure in both nitrogen and air environments and qualify the impact of different failure mitigation strategies. 18650 LCO cells were tested, and during each test, one cell would intentionally be forced into thermal runaway. As the failure propagated throughout the array, temperatures of the cells' bottom surfaces, temperature of the gas stream, and species concentrations of the gas stream were all measured.

In all cases, the failure tended to propagate on a row-to-row basis, but the speeds of propagation varied depending on the test configuration. On average, tests conducted in air propagated roughly 7.5 times faster than equivalent tests conducted in nitrogen, and tests conducted at 50% SOC propagated roughly 8.5 times slower than equivalent tests conducted at 100% SOC. The presence of a 5 mm gap between rows slowed the propagation speed to roughly three times less than it was without the gap. The failure onset and maximum temperatures were not impacted at all by the 5 mm gap and were only minimally impacted by ambient environment. Decreasing the SOC to 50%, however, did dramatically alter these temperatures, increasing the thermal runaway onset temperature by roughly 70 K and decreasing the maximum temperature by roughly 50 K.

With and without the 5 mm gap, 100% SOC cells tested in nitrogen lost about 38% of their initial mass during failure. This value increased slightly to 41.5% in the air tests and decreased significantly to 19.2% in the 50% SOC tests. The average number of ruptured cells in each test followed similar trends. Gas analysis from the nitrogen tests confirmed the formation of small mass yields of O_2 and H_2 during failure, as well as large mass yields of THC, CO, and CO_2. Additionally, the total measured gas mass yield was approximately 4.3 times greater for the 12 cell tests at 100% SOC than it was for the 12 cell tests at 50% SOC. These mass yields resulted in LFL values of about 5.7% and 4.9% for cells at 100% SOC and 50% SOC, respectively. The maximum air volume in which the ejected gases from a single cell form a flammable mixture was estimated to be 3.3 times smaller for a 50% SOC cell than a 100% SOC cell.

Chemical heat generation during failure in the nitrogen tests was determined to be approximately 59 kJ per failed cell in the 100% SOC tests (both with and without the 5 mm gaps), but only 36 kJ per failed cell in the 50% SOC tests. When normalized by the stored electrical energy of a cell, however, the 50% SOC cells produced more energy than the 100% SOC cells. For the wind tunnel air tests, flaming combustion energy was calculated to be approximately 63 kJ per failed cell. This value represents a plausible and likely energy production in a real scenario, but was the result of significant incomplete combustion. Using a modified CSBC apparatus, a more complete combustion scenario was tested, and a flaming combustion energy value of approximately 107 kJ per failed cell was calculated.

Overall, the LIB cell arrays were more hazardous in the reactive environment than they were in the inert environment. Not only did the heat production during failure more than double, due to the introduction of combustion, but the propagation of failure also sped up significantly, and even appeared to possibly accelerate throughout the array. Installing battery packs in a pure nitrogen (or other inert) environment can be costly and is rather impractical for most small consumer electronics, but when being stored or transported, an inert system can be an impactful safety strategy when combined with other mitigation approaches. Decreasing the SOC of the cells also showed significant promise in regards to failure mitigation. While unable to halt failure propagation completely, decreasing the SOC to 50% did significantly slow the propagation and decrease the cell temperatures, yields of ejected hazardous gases, and chemical heat production. Limiting operating cells to 50% SOC is impractical for performance reasons, but when being stored or transported, decreasing SOC to 50% is a simple solution that makes the battery pack significantly less hazardous. Introducing 5 mm gaps between certain rows of cells was less effective. Cell temperatures, gas yields, and energy production were not affected at all, and propagation speed was only impacted to a moderate (and somewhat inconclusive) degree. Introducing gaps between cell modules is the only mitigation strategy tested that is feasible for operating, small scale systems, however. Every gap that is introduced may somewhat slow failure propagation, but they also increase the size and worsen the space optimization of the pack at the same time. None of these mitigation strategies were able to sufficiently eliminate the cascading failure hazards altogether, however. Failure propagation was not prevented in any test, so different mitigation strategies or the combination of multiple mitigation strategies need to be studied before any definitive safety recommendations can be made.

5.2 Future Work

Additional tests, similar to those in this investigation, should be conducted to strengthen the conclusions made. Given the apparent influence of SOC on failure phenomena, tests at additional SOCs should be conducted. Perhaps cells at 70% or 80% SOC do not offer much benefit over 100% SOC cells, or perhaps there exists a critical SOC below which thermal runaway will not propagate. Similarly, there may exist a critical gap size or number of gaps within a cell array that can sufficiently reduce the heat transfer and halt the thermal runaway propagation. Many additional tests would be required to make these conclusions.

Given that the 5 mm gap tests were unable to prevent thermal runaway propagation, the current study should be expanded upon by introducing thermal barriers into the gaps. Many different types of barriers should be tested, even simple barriers such as Kaowool PM insulation. Some of them may be able to reduce the cell-to-cell heat transfer sufficiently enough that failure propagation is stopped.

The experimental facility used for testing also offers many customization options that were not utilized in the current study. Array size, cathode chemistry, nominal capacity, form factor, electrical connection method, and suppression strategy were all kept constant, but the cell holder and wind tunnel have the functionality to incorporate these variables. Any of these variables could dramatically impact the safety hazards that LIB cell arrays pose, so a thorough investigation into any of them would be of merit.

Despite the variability of the experimental facility, it does have some limitations. The size of the facility and capabilities of the laboratory limit the number of cells that can be tested at the same time. Additionally, altering form factor and cell arrangement is possible, but also time consuming and costly because a new bottom plate would have to be manufactured for every alteration. In order to quickly and inexpensively investigate these test configurations, a 3D, CFD model should be developed that could accurately predict the times and temperatures of failure of every cell within an array. The experimental results outlined here could be used to validate and potentially parametrize the model. Once the boundary conditions, chemical reactions, and heat transfer are accurately modeled, many complex scenarios that are not feasible in the current experimental facility could be studied.

Appendices

A.1 Example Cell Temperatures

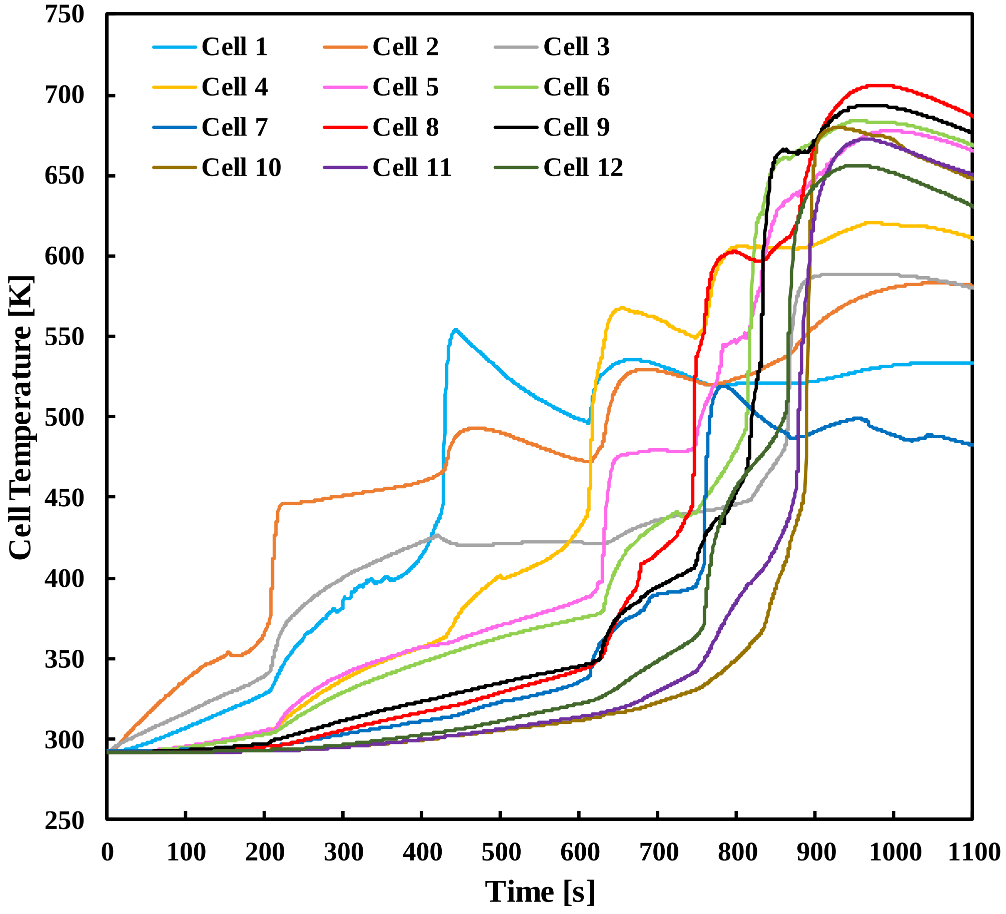

Figure A.1: Example cell thermocouple measurements from all cells in a 12 cell, 50% SOC test in N_2.

A.2 Visual Appearance of Thermal Runaway

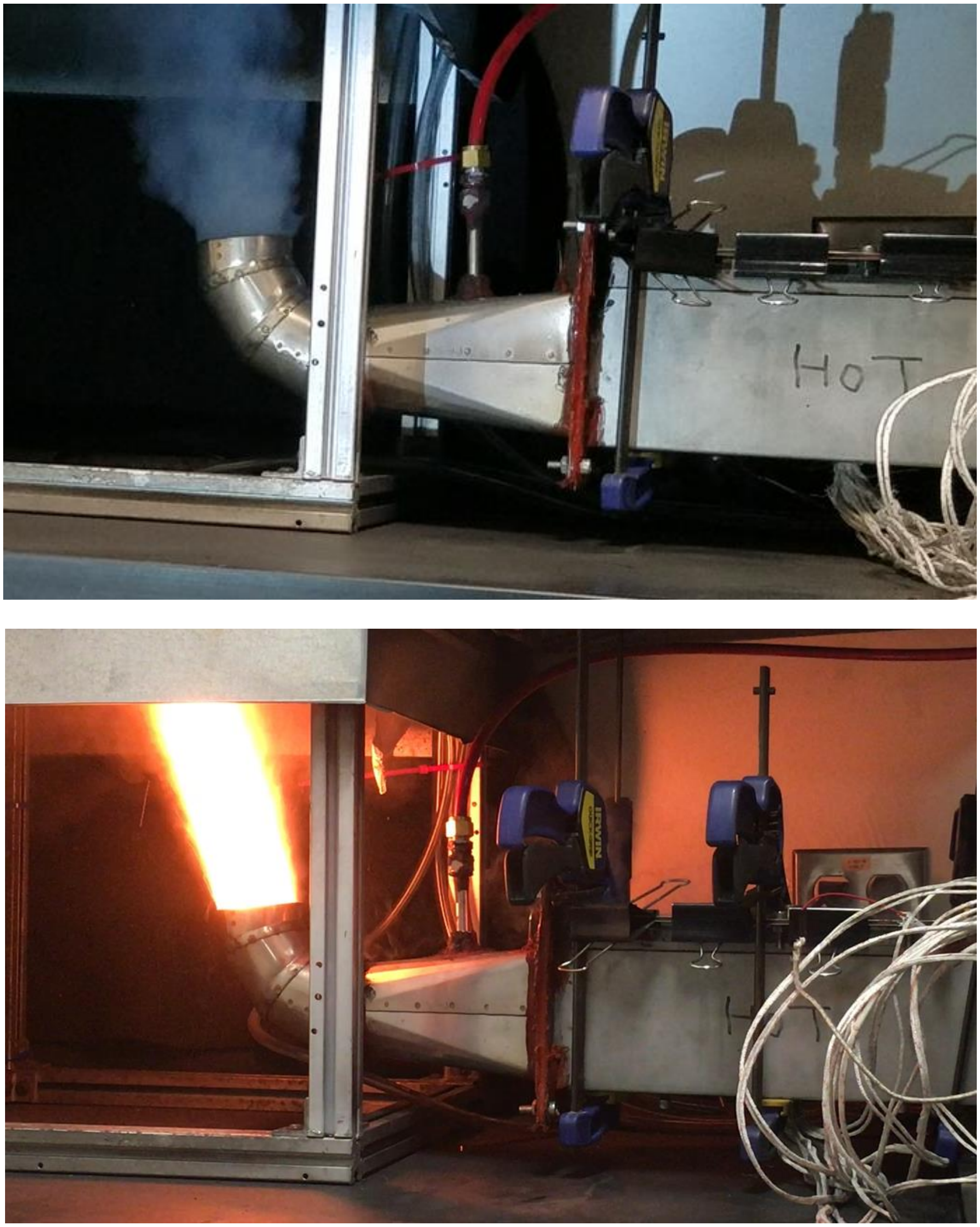

Figure A.2: Visual observations during thermal runaway in an N_2 test (top) and an air test (bottom). A flammable gas plume coming from the exhaust elbow is visible in the N_2 tests. The plume ignites in the air tests, resulting in a visible flame jet.

Bibliography

[1] P. Poizot, F. Dolhem. Clean energy new deal for a sustainable world: from non-CO_2 generating energy sources to greener electrochemical storage devices. *Energy & Environmental Science*, 4:2003–2019, 2011.

[2] T.B. Reddy. *Linden's Handbook of Batteries, Fourth Edition*. McGraw-Hill Education, New York, NY, 2011.

[3] P.G. Balakrishnan, R. Ramesh, T.P. Kumar. Safety mechanisms in lithium-ion batteries. *Journal of Power Sources*, 155:401–414, 2006.

[4] Q. Wang, P. Ping, X. Zhao, G. Chu, J. Sun, C. Chen. Thermal runaway caused fire and explosion of lithium ion battery. *Journal of Power Sources*, 208:210–224, 2012.

[5] T.M. Bandhauer, S. Garimella, T.F. Fuller. A Critical Review of Thermal Issues in Lithium-Ion Batteries. *Journal of The Electrochemical Society*, 158(3):R1–R25, 2011.

[6] J. Swartz. Samsung recalls 1M Samsung Galaxy Note 7 phones. *USA Today*, 2016.

[7] C. Lo. Smoke from mobile phone battery sends two Hong Kong Apple store employees to hospital. *South China Morning Post*, 2018.

[8] V. Ryckart. Tesla crash scene posed risks for firefighters. *USA Today*, 2017.

[9] V. Kapur. UPS Dubai crash: GCAA final report links accident to lithium batteries. *Emirates 24|7 News*, 2013.

[10] R. Wingfield-Hayes. Dreamliner: Boeing 787 planes grounded on safety fears. *BBC News*, 2013.

[11] Batteries Carried by Airline Passengers Frequently Asked Questions. Federal Aviation Administration, Office of Hazardous Materials Safety, 2016.

[12] H. Yang, H. Bang, K. Amine, J. Prakash. Investigations of the Exothermic Reactions of Natural Graphite Anode for Li-Ion Batteries during Thermal Runaway. *Journal of The Electrochemical Society*, 152(1):A73–A79, 2005.

[13] H. Maleki, G. Deng, A. Anani, J. Howard. Thermal Stability Studies of Li-Ion Cells and Components. *Journal of The Electrochemical Society*, 146(9):3224–3229, 1999.

[14] Y.S. Duh, C.Y. Lee, Y.L. Chen, C.S. Kao. Characterization on the exothermic behaviors of cathode materials reacted with ethylene carbonate in lithium-ion battery studied by differential scanning calorimeter (DSC). *Thermochimica Acta*, 642:88–94, 2016.

[15] E.P. Roth, D.H. Doughty, J. Franklin. DSC investigation of exothermic reactions occurring at elevated temperatures in lithium-ion anodes containing PVDF-based binders. *Journal of Power Sources*, 134:222–234, 2004.

[16] E.P. Roth, D.H. Doughty. Thermal abuse performance of high-power 18650 Li-ion cells. *Journal of Power Sources*, 128:308–318, 2004.

[17] U. von Sacken, E. Nodwell, A. Sundher, J.R. Dahn. Comparative thermal stability of carbon intercalation anodes and lithium metal anodes for rechargeable lithium batteries. *Journal of Power Sources*, 54:240–245, 1995.

[18] S. Al Hallaj, H. Maleki, J.S. Hong, J.R. Selman. Thermal modeling and design considerations of lithium-ion batteries. *Journal of Power Sources*, 83:1–8, 1999.

[19] H. Maleki, J.N. Howard. Role of the cathode and anode in heat generation of Li-ion cells as a function of state of charge. *Journal of Power Sources*, 137:117–127, 2004.

[20] R.E. Lyon, R.N. Walters. Energetics of lithium ion battery failure. *Journal of Hazardous Materials*, 318:164–172, 2016.

[21] R.N. Walters, R.E. Lyon. Measuring Energy Release of Lithium-ion Battery Failure Using a Bomb Calorimeter. DOT/FAA/TC-15/40, 2016.

[22] X. Liu, S.I. Stoliarov, M. Denlinger, A. Masias, K. Snyder. Comprehensive calorimetry of the thermally-induced failure of a lithium ion battery. *Journal of Power Sources*, 280:516–525, 2015.

[23] X. Liu, Z. Wu, S.I. Stoliarov, M. Denlinger, A. Masias, K. Snyder. Heat release during thermally-induced failure of a lithium ion battery: Impact of cathode composition. *Fire Safety Journal*, 85:10–22, 2016.

[24] X. Liu. Comprehensive calorimetry and modeling of the thermally-induced failure of a lithium ion battery. Doctor of Philosophy, University of Maryland, 2016.

[25] J.G. Quintiere, S.B. Crowley, R.N. Walters, R.E. Lyon, D. Blake. Fire Hazards of Lithium Batteries. DOT/FAA/TC-TN15/17, 2016.

[26] A.O. Said, C. Lee, X. Liu, Z. Wu, S.I. Stoliarov. Simultaneous measurement of multiple thermal hazards associated with a failure of prismatic lithium ion battery. *Proceedings of the Combustion Institute*, 2018. DOI: 10.1016/j.proci.2018.05.066.

[27] Q. Wang, P. Huang, P. Ping, Y. Du, K. Li, J. Sun. Combustion behavior of lithium ion phosphate battery induced by external heat radiation. *Journal of Loss Prevention in the Process Industries*, 49:961–969, 2017.

[28] P. Ping, Q. Wang, P. Huang, K. Li, J. Sun, D. Kong, C. Chen. Study of the fire behavior of high-energy lithium-ion batteries with full-scale burning test. *Journal of Power Sources*, 285:80–89, 2015.

[29] P. Ribière, S. Grugeon, M. Morcrette, S. Boyanov, S. Laruelle, G. Marlair. Investigation on the fire-induced hazards of Li-ion battery cells by fire calorimetry. *Energy & Environmental Science*, 5:5271–5280, 2012.

[30] F. Larsson, P. Andersson, P. Blomqvist, A. Lorén, B.E. Mellander. Characteristics of lithium-ion batteries during fire tests. *Journal of Power Sources*, 271:414–420, 2014.

[31] P. Andersson, P. Blomqvist, A. Lorén, F. Larsson. Using Fourier transform infrared spectroscopy to determine toxic gases in fires with lithium-ion batteries. *Fire and Materials*, 40:999–1015, 2016.

[32] F. Larsson, S. Bertilsson, M. Furlani, I. Albinsson, B.E. Mellander. Gas explosions and thermal runaways during external heating abuse of commercial lithium-ion graphite-$LiCoO_2$ cells at different levels of aging. *Journal of Power Souces*, 373:220–231, 2018.

[33] Y. Fernandes, A. Bry, S. de Persis. Identification and quantification of gases emitted during abuse tests by overcharge of a commercial Li-ion battery. *Journal of Power Sources*, 389:106–119, 2018.

[34] J. Sun, J. Li, T. Zhou, K. Yang, S. Wei, N. Tang, N. Dang, H. Li, X. Qiu, L. Chen. Toxicity, a serious concern of thermal runaway from commercial Li-ion battery. *Nano Energy*, 27:313–319, 2016.

[35] S. Bertilsson, F. Larsson, M. Furlani, I. Albinsson, B.E. Mellander. Lithium-ion battery electrolyte emissions analyzed by coupled thermogravimetric/Fourier-transform infrared spectroscopy. *Journal of Power Sources*, 365:446–455, 2017.

[36] T. Maloney. Lithium Battery Thermal Runaway Vent Gas Analysis. DOT/FAA/TC-15/59, 2016.

[37] R. Sabbah, R. Kizilel, J.R. Selman, S. Al-Hallaj. Active (air-cooled) vs. passive (phase change material) thermal management of high power lithium-ion packs: Limitation of temperature rise and uniformity of temperature distribution. *Journal of Power Sources*, 182:630–638, 2008.

[38] X. Li, F. He, L. Ma. Thermal management of cylindrical batteries investigated using wind tunnel testing and computational fluid dynamics simulation. *Journal of Power Sources*, 238:395–402, 2013.

[39] N. Yang, X. Zhang, G. Li, D. Hua. Assessment of the forced air-cooling performance for cylindrical lithium-ion battery packs: A comparative analysis between aligned and staggered cell arrangements. *Applied Thermal Engineering*, 80:55–65, 2015.

[40] R. Kizilel, A. Lateef, R. Sabbah, M.M. Farid, J.R. Selman, S. Al-Hallaj. Passive control of temperature excursion and uniformity in high-energy Li-ion battery

packs at high current and ambient temperature. *Journal of Power Sources*, 183:370–375, 2008.

[41] C.F. Lopez, J.A. Jeevarajan, P.P. Mukherjee. Experimental Analysis of Thermal Runaway and Propagation of Lithium-Ion Battery Modules. *Journal of The Electrochemical Society*, 162(9):A1905–A1915, 2015.

[42] J. Lamb, C.J. Orendorff, L.A.M. Steele, S.W. Spangler. Failure propagation in multi-cell lithium ion batteries. *Journal of Power Sources*, 283:517–523, 2015.

[43] X. Feng, J. Sun, M. Ouyang, F. Wang, X. He, L. Lu, H. Peng. Characterization of penetration induced thermal runaway propagation process within a large format lithium ion battery module. *Journal of Power Sources*, 275:261–273, 2015.

[44] X. Feng, L. Lu, M. Ouyang, J. Li, X. He. A 3D thermal runaway propagation model for a large format lithium ion battery module. *Energy*, 115:194–208, 2016.

[45] X. Feng, X. He, M. Ouyang, L. Lu, P. Wu, C. Kulp, S. Prasser. Thermal runaway propagation model for designing a safer battery pack with 25 Ah $LiNi_xCo_yMn_zO_2$ large format lithium ion battery. *Applied Energy*, 74–91, 2015.

[46] T. Wang, K.J. Tseng, J. Zhao, Z. Wei. Thermal investigation of lithium-ion battery module with different cell arrangement structures and forced air-cooling strategies. *Applied Energy*, 134:229–238, 2014.

[47] R.M. Spotnitz, J. Weaver, G. Yeduvaka, D.H. Doughty, E.P. Roth. Simulation of abuse tolerance of lithium-ion battery packs. *Journal of Power Sources*, 163:1080–1086, 2007.

[48] B. Coleman, J. Ostanek, J. Heinzel. Reducing cell-to-cell spacing for large-format lithium ion battery modules with aluminum or PCM heat sinks under failure conditions. *Applied Energy*, 180:14–26, 2016.

[49] Tenergy ICR18650 Lithium Ion Battery Specification Approval Sheet. Tenergy, Fremont, CA, 2010.

[50] T.L. Bergman, A.S. Lavine, F.P. Incropera, D.P. Dewitt. *Fundamentals of Heat and Mass Transfer, Seventh Edition*. John Wiley & Sons, Hoboken, NJ, 2011.

[51] ASTM Standard E1354-17, Standard Test Method for Heat and Visible Smoke Release Rates for Materials and Products Using an Oxygen Consumption Calorimeter. ASTM International, West Conshohocken, PA, 2017.

[52] Lithium Battery Guidance Document. International Air Transport Association, Montreal, Canada, 2016.

[53] S. McAllister, J. Chen, A.C. Fernandez-Pello. *Fundamentals of Combustion Processes*. Springer, New York, NY, 2011.

[54] C. Borgnakke, R.E. Sonntag. *Fundamentals of Thermodynamics, Seventh Edition*. John Wiley & Sons, Hoboken, NJ, 2009.

[55] A.T.D. Butland, R.J. Maddison. The Specific Heat of Graphite: An Evaluation of Measurements. *Journal of Nuclear Materials*, 49:45–56, 1973.

[56] I.T. Leventon, J. Li, S.I. Stoliarov. A flame spread simulation based on a comprehensive solid pyrolysis model coupled with a detailed empirical flame structure representation. *Combustion and Flame*, 162:3884–3895, 2015.